Mon. Not. R. Astron. Soc. **000**, 1–22 (2014) Printed 26 March 2014 (MN LATEX style file v2.2)

Non-equilibrium chemistry and cooling in the diffuse interstellar medium - II. Shielded gas

A. J. Richings[1], J. Schaye[1] and B. D. Oppenheimer[2]
[1] *Leiden Observatory, Leiden University, PO Box 9513, 2300 RA Leiden, the Netherlands*
[2] *Center for Astrophysics and Space Astronomy, Department of Astrophysical and Planetary Sciences, University of Colorado, 389 UCB, Boulder, CO 80309, USA*

arXiv:1403.6155v1 [astro-ph.GA] 24 Mar 2014

26 March 2014

ABSTRACT

We extend the non-equilibrium model for the chemical and thermal evolution of diffuse interstellar gas presented in Richings et al. (2014) to account for shielding from the UV radiation field. We attenuate the photochemical rates by dust and by the gas itself, including absorption by HI, H_2, HeI, HeII and CO where appropriate. We then use this model to investigate the dominant cooling and heating processes in interstellar gas as it becomes shielded from the UV radiation. We consider a one-dimensional plane-parallel slab of gas irradiated by the interstellar radiation field, either at constant density and temperature or in thermal and pressure equilibrium. The dominant thermal processes tend to form three distinct regions in the clouds. At low column densities cooling is dominated by ionised metals such as SiII, FeII, FeIII and CII, which are balanced by photoheating, primarily from HI. Once the hydrogen-ionising radiation becomes attenuated by neutral hydrogen, photoelectric dust heating dominates, while CII becomes dominant for cooling. Finally, dust shielding triggers the formation of CO and suppresses photoelectric heating. The dominant coolants in this fully shielded region are H_2 and CO. We find that the transition from atomic to molecular hydrogen is triggered by H_2 self-shielding. The transition column density is lower at higher density (or at higher pressure for gas clouds in pressure equilibrium) and at higher metallicity, due to an increase in the H_2 fraction in the photodissociated region and hence a corresponding increase in the H_2 self-shielding. We also compare the HI-H_2 transition in our model to two prescriptions for molecular hydrogen formation that have been implemented in hydrodynamic simulations.

Key words: astrochemistry - ISM: atoms - ISM: clouds - ISM: molecules - molecular processes - galaxies: ISM.

1 INTRODUCTION

The thermal evolution of gas is an important component of hydrodynamic simulations of galaxy formation as it determines how quickly the gas can cool and collapse to form dense structures, and ultimately stars. The star formation in such simulations can be limited to the cold phase of the interstellar medium (ISM) if we have sufficient resolution to resolve the Jeans mass ($M_J \propto \rho^{-1/2} T^{3/2}$) in the cold gas. It is desirable to include a multi-phase treatment of the ISM, as this will produce a more realistic description of the distribution of star formation within the galaxy, along with the resulting impact of stellar feedback on the ISM and the galaxy as a whole (e.g. Ceverino & Klypin 2009; Governato et al. 2010; Halle & Combes 2013; Hopkins et al. 2013). Therefore, it is important that we correctly follow the thermal evolution of gas between the warm ($T \sim 10^4$ K) and cold ($T \lesssim 100$ K) phases of the ISM in these simulations.

The radiative cooling rate depends on the chemical abundances in the gas, including the ionisation balance, and hence on its chemical evolution. However, following the full non-equilibrium chemistry of the ISM within a hydrodynamic simulation can be computationally expensive, as it requires us to integrate a system of stiff differential equations that involves hundreds of species and thousands of reactions. Therefore, many existing cosmological hydrodynamic simulations use tabulated cooling rates assuming chemical (including ionisation) equilibrium. For example, the cosmological simulations that were run as part of the OverWhelmingly Large Simulations project (OWLS; Schaye et al. 2010) use the pre-computed cooling functions of Wiersma et al. (2009),

© 2014 RAS

which were calculated using CLOUDY[1] (Ferland et al. 1998, 2013) as a function of temperature, density and abundances of individual elements assuming ionisation equilibrium in the presence of the Haardt & Madau (2001) extragalactic UV background. However, this assumption of ionisation equilibrium may not remain valid if the cooling or dynamical time-scale becomes short compared to the chemical time-scale (e.g. Kafatos 1973; Gnat & Sternberg 2007; Oppenheimer & Schaye 2013a; Vasiliev 2013) or if the UV radiation field is varying in time (e.g. Oppenheimer & Schaye 2013b).

In the first paper of this series (Richings et al. 2014; hereafter paper I) we presented a chemical network to follow the non-equilibrium thermal and chemical evolution of interstellar gas. Using this model we investigated the chemistry and cooling properties of optically thin interstellar gas in the ISM and identified the dominant coolants for gas exposed to various UV radiation fields. We also looked at the impact that non-equilibrium chemistry can have on the cooling rates and chemical abundances of such gas.

In this paper we extend our thermo-chemical model to account for gas that is shielded from the incident UV radiation field by some known column density. We focus on physical conditions with densities $10^{-2}\,\mathrm{cm}^{-3} \lesssim n_{\mathrm{H_{tot}}} \lesssim 10^{4}\,\mathrm{cm}^{-3}$ and temperatures of $10^{2}\,\mathrm{K} \lesssim T \lesssim 10^{4}\,\mathrm{K}$. This is most relevant to gas that is cooling from the warm phase to the cold phase of the ISM. We apply our model to a one-dimensional plane-parallel slab of gas that is irradiated by the Black (1987) interstellar radiation field to investigate how the chemistry and cooling properties of the gas change as it becomes shielded from the UV radiation, both by dust and by the gas itself. The spectral shape of the radiation field will change with the depth into the cloud as high energy photons are able to penetrate deeper. Hence, the major coolants and heating processes will vary with column density. Such one-dimensional models are commonly used to model photodissociation regions (PDRs) and diffuse and dense clouds (e.g. Tielens & Hollenbach 1985; van Dishoeck & Black 1986, 1988; Visser et al. 2009; Wolfire et al. 2010).

It has been suggested recently that the star formation rate of galaxies may be more strongly correlated to the molecular gas content than to atomic hydrogen (Wong & Blitz 2002; Schaye 2004; Kennicutt et al. 2007; Leroy et al. 2008; Bigiel et al. 2008, 2010), although the more fundamental and physically relevant correlation may be with the cold gas content (Schaye 2004; Krumholz et al. 2011; Glover & Clark 2012). Motivated by this link between molecular hydrogen and star formation, a number of studies have implemented simple methods to follow the abundance of H_2 in numerical simulations of galaxies (e.g. Pelupessy et al. 2006; Gnedin et al. 2009; McKee & Krumholz 2010; Christensen et al. 2012). We compare the H_2 fractions predicted by some of these methods to those calculated using our model to investigate the physical processes that determine the HI-H_2 transition and to explore in which physical regimes these various prescriptions remain valid.

Throughout this paper we use the default solar abundances assumed by CLOUDY, version 13.01 (see for example table 1 in Wiersma et al. 2009). In particular, we take the solar metallicity to be $Z_{\odot} = 0.0129$. This paper is organised as follows. In section 2 we summarise the thermo-chemical model presented in paper I, and in section 3 we describe how the photochemical rates are attenuated by dust and gas. We look at the photoionisation rates in section 3.1, the photodissociation of molecular species in section 3.2 and the photoheating rates in section 3.3. In section 4 we apply this model to a one-dimensional plane-parallel slab of gas to investigate the chemistry and cooling properties of the gas as it becomes shielded from the UV radiation field, and we compare these results with CLOUDY. In section 5 we compare the time-dependent molecular H_2 fractions predicted by our model with two prescriptions for H_2 formation taken from the literature that have been implemented in hydrodynamic simulations. Finally, we discuss our results and conclusions in section 6.

[1] `http://nublado.org/`

2 THERMO-CHEMICAL MODEL

In this section we give a brief overview of the chemical and thermal processes that are included in our model. These are described in more detail in paper I.

We follow the evolution of 157 chemical species, including 20 molecules (H_2, H_2^+, H_3^+, OH, H_2O, C_2, O_2, HCO^+, CH, CH_2, CH_3^+, CO, CH^+, CH_2^+, OH^+, H_2O^+, H_3O^+, CO^+, HOC^+ and O_2^+) along with electrons and all ionisation states of the 11 elements that dominate the cooling rate (H, He, C, N, O, Ne, Si, Mg, S, Ca and Fe). The rate equations of these species and the equation for the temperature evolution give us a system of 158 differential equations that we integrate from the initial conditions with CVODE (a part of the SUNDIALS[2] suite of non-linear differential/algebraic equation solvers), using the backward difference formula method and Newton iteration.

2.1 Chemistry

Our chemical network contains 907 reactions, including:

Collisional reactions. We include the collisional ionisation, radiative and di-electronic recombination and charge transfer reactions of all ionisation states of the 11 elements in our network. The rate coefficients of these reactions were tabulated as a function of temperature by Oppenheimer & Schaye (2013a) using CLOUDY (they use version 10.00, but they have since produced updated versions of these tables using version 13.01 of CLOUDY[3]). We also include reactions for the formation and destruction of molecular hydrogen taken from Glover & Jappsen (2007); Glover & Abel (2008) and others, and the CO network from Glover et al. (2010) with some small modifications (see section 2.5 of paper I).

Photochemical reactions. We compute the optically thin photoionisation rates using the grey approximation cross sections of each atom and ion species for a given UV spectrum, which we calculate using the frequency dependent cross sections from Verner & Yakovlev (1995) and Verner et al. (1996). We also include Auger ionisation, where photoionisation of inner shell electrons can lead to the ejection

[2] `https://computation.llnl.gov/casc/sundials/main.html`

[3] These updated tables are available on the website: `http://noneq.strw.leidenuniv.nl`

of multiple electrons by a single photon. For these we use the electron vacancy distribution probabilities from Kaastra & Mewe (1993). We assume that the optically thin photodissociation rate of molecular hydrogen scales linearly with the number density of photons in the energy band $12.24\,\mathrm{eV} < h\nu < 13.51\,\mathrm{eV}$, normalised to the photodissociation rate in the presence of the Black (1987) interstellar radiation field calculated by Cloudy (see section 2.2.2 of paper I). For the remaining molecular species, we use the photoionisation and photodissociation rates given by van Dishoeck et al. (2006) and Visser et al. (2009) where available, or Glover et al. (2010) otherwise. In paper I we only considered optically thin gas. In section 3 we describe how we modify these optically thin rates for shielded gas.

Cosmic ray ionisation. The ionisation rate of HI due to cosmic rays, ζ_{HI}, is a free parameter in our model. We use a default value of $\zeta_{\mathrm{HI}} = 2.5 \times 10^{-17}\,\mathrm{s}^{-1}$ (Williams et al. 1998). The cosmic ray ionisation rates of the other species are then scaled linearly with this parameter. The ratio of the ionisation rate of each species with respect to HI is assumed to be equal to the ratio of these ionisation rates given in the UMIST database[4] (Le Teuff et al. 2000) where available. For species that do not appear in this database, we calculate their cosmic ray ionisation rate with respect to ζ_{HI} using Lotz (1967), Silk (1970) and Langer (1978). For the molecular species, we use the cosmic ray ionisation and dissociation rates from table B3 of Glover et al. (2010), again scaled with ζ_{HI}.

Dust grain reactions. The formation rate of molecular hydrogen on dust grains is calculated using equation 18 from Cazaux & Tielens (2002). We take a constant dust temperature $T_{\mathrm{dust}} = 10$ K, which we find has a negligible impact on our results, and we assume that the abundance of dust scales linearly with metallicity. We also include a small number of recombination reactions on dust grains, taken from Weingartner & Draine (2001a).

2.2 Thermal processes

For a complete list of cooling and heating processes in our model, see table 1 of paper I. Below we summarise some of the cooling and heating mechanisms that are most important in the diffuse ISM.

Metal-line cooling. Oppenheimer & Schaye (2013a) tabulate the radiative cooling rates of all ionisation states of the 11 elements in our chemical network as a function of temperature, calculated using Cloudy (as for the rate coefficients, they use version 10.00, but they have since produced updated versions of these tables using version 13.01 of Cloudy[3]). We use these cooling rates for most metal species in our model. However, these rates assume that the radiative cooling is dominated by electron-ion collisions. For a small number of species this assumption can break down at low temperatures ($T \lesssim 10^3$ K). We therefore found it necessary to calculate the cooling rates of OI and CI as a function of temperature and of HI, HII and electron densities, using the same method as Glover & Jappsen (2007). This enables us to follow the radiative cooling rates of these species in regimes that are dominated by collisions with HI or HII, as well as when electron-ion collisions dominate. We also tabulated the cooling rates of CII, NII, SiII and FeII as functions of temperature and electron density using version 7.1 of the Chianti database[5] (Dere et al 1997; Landi et al 2013).

H_2 rovibrational cooling. We use the H_2 cooling function from Glover & Abel (2008), assuming an ortho- to para-ratio of 3:1. This includes collisional excitation of the rovibrational levels of molecular hydrogen by HI, HII, H_2, HeI and electrons.

Photoheating. We calculate the average excess energy of ionising photons for each species, given the incident UV spectrum, using the frequency dependent cross sections from Verner & Yakovlev (1995) and Verner et al. (1996). We then multiply these by the corresponding photoionisation rate to obtain the photoheating rate for each species. See section 3.3 for a description of how we modify these optically thin photoheating rates for shielded gas.

Photoelectric heating. The absorption of UV photons by dust grains can release electrons, and the excess energy that is absorbed by the electrons is quickly thermalised, which heats the gas. We calculate the photoelectric heating rate from dust grains using equations 1 and 2 from Wolfire et al. (1995).

3 SHIELDING PROCESSES

In paper I we considered only optically thin gas. However, for shielded gas we need to consider how both the intensity and the shape of the UV spectrum change as the radiation field becomes attenuated by both dust and the gas itself. The photochemical rates presented in paper I involve integrals over photon frequency, but these are expensive to compute. For the optically thin rates we use the grey approximation to pre-compute these integrals, so that they do not need to be re-evaluated at every timestep in the chemistry solver. However, this approximation becomes invalid if the shape of the UV spectrum is no longer invariant.

In the following sections we describe how we modify the optically thin rates of photoionisation, photodissociation and photoheating for gas that is shielded by a known column density. To implement these methods in a hydrodynamic simulation, we would need to estimate this column density for each gas particle/cell. This is typically done by assuming that shielding occurs locally over some characteristic length scale L, so that the column density N_i of a gas cell with density n_i can be estimated from local quantities as:

$$N_i = n_i L. \tag{3.1}$$

If the macroscopic velocity gradient dv/dr is large with respect to local variations in the thermal line broadening, for example in turbulent molecular clouds, we can use the Sobolev length (Sobolev 1957), which gives the length scale over which the Doppler shift of a line due to the velocity gradient is equal to the thermal width of the line:

[4] `http://www.udfa.net`

[5] `http://www.chiantidatabase.org/chianti.html`

$$L_{\rm Sob} = \frac{v_{\rm th}}{|dv/dr|}, \tag{3.2}$$

where $v_{\rm th}$ is the thermal velocity. This method is applicable to the shielding of individual lines, for example in the self-shielding of molecular hydrogen. Gnedin et al. (2009) use a Sobolev-like approximation to estimate the column density using the density gradient rather than the velocity gradient:

$$L_{{\rm Sob},\rho} = \frac{\rho}{|\nabla\rho|}. \tag{3.3}$$

By integrating column densities along random lines of sight in their cosmological simulations, in which they are able to resolve individual giant molecular complexes, Gnedin et al. (2009) confirm that this approximation reproduces the true column density with a scatter of a factor ~ 2 in the range $3 \times 10^{20}\,{\rm cm}^{-2} < N_{\rm HI} + 2N_{\rm H_2} < 3 \times 10^{23}\,{\rm cm}^{-2}$ (see their figure 1).

An alternative approach is to assume that shielding occurs locally on scales of the Jeans length, $L_{\rm Jeans}$ (Schaye 2001a,b; Rahmati et al. 2013). For example, Hopkins et al. (2013) integrate the density out to $L_{\rm Jeans}$ for each particle to obtain its shielding column density, which they use to attenuate the UV background.

Wolcott-Green et al. (2011) use these three methods to estimate the self-shielding of molecular hydrogen and compare them to their calculations of the radiative transfer of Lyman Werner radiation through simulated haloes at redshift $z \sim 10$. They find that using the Sobolev length (equation 3.2) is the most accurate method based only on local properties, compared to their radiative transfer calculations.

Our chemical model could also be coupled to a full 3D radiative transfer simulation, in which the shielding of the UV radiation is computed by the radiative transfer solver rather than using the methods that we describe below. However, to include the impact of shielding on the shape of the UV spectrum, we require multiple frequency bins, as the spectral shape is assumed to remain constant within individual frequency bins. Such a calculation is likely to be computationally expensive. In a future work we shall compare our methods described below, with different approximations for the column density, to radiative transfer calculations to investigate in which physical conditions these various approximations can be applied in hydrodynamic simulations.

3.1 Photoionisation

The incident UV radiation field is attenuated by both dust and gas. The factor by which dust reduces the photoionisation rate of a species can be written as:

$$S^i_{\rm d} = \exp(-\gamma^i_{\rm d} A_v) = \exp\left(-4.0 \times 10^{-22} \gamma^i_{\rm d} N_{\rm H_{tot}} Z/Z_\odot\right), \tag{3.4}$$

where we can express this factor in terms of the visual extinction A_v or the total intervening hydrogen column density $N_{\rm H_{tot}} = N_{\rm HI} + N_{\rm HII} + 2N_{\rm H_2}$. Following Krumholz et al. (2011), we use $A_v/N_{\rm H_{tot}} = 4.0 \times 10^{-22} Z/Z_\odot$ mag cm^2, which is intermediate between the values from the models of Weingartner & Draine (2001b) for the Milky Way (with a visual extinction to reddening ratio $R_v = 3.1$ or 5.5), the Large Magellanic Cloud and the Small Magellanic Cloud, and assumes that the dust content of the gas scales linearly with its metallicity. The factor γ^i_d is a constant that is different for each species and depends on the range of photon energies that ionise that species. This factor accounts for the fact that the absorbing cross section of dust grains varies with photon energy, so the effective dust column density depends on which energy range we are interested in. We use the values for γ^i_d calculated for the Draine (1978) interstellar radiation field from table 3 of van Dishoeck et al. (2006) where available, or from table B2 of Glover et al. (2010) otherwise. Since CaI and CaII were not included in either reference, we simply use the value of γ^i_d from species that have similar ionisation energies (MgI and CI respectively).

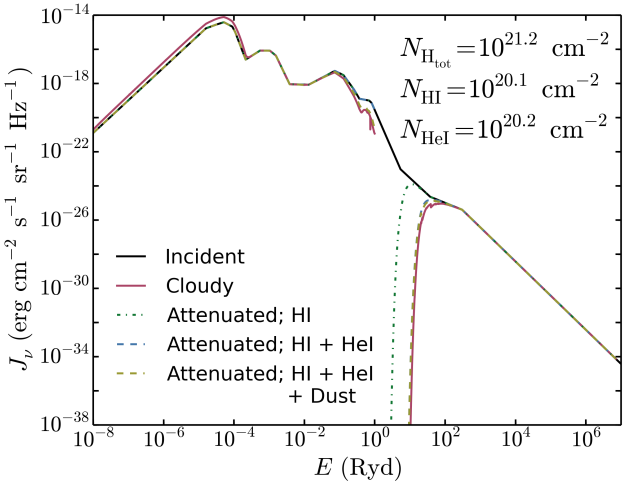

Figure 1. The effect of dust and gas shielding on the radiation spectrum. The incident spectrum of the Black (1987) interstellar radiation field is shown by the black curve, and the coloured curves show the resulting spectrum after it has passed through a total hydrogen column density $N_{\rm H_{tot}} = 1.6 \times 10^{21}$ cm^{-2} at solar metallicity, as calculated by CLOUDY, and the spectrum attenuated only by HI, by HI and HeI, and by HI, HeI and dust.

While dust is the dominant source of absorption of UV radiation below 13.6 eV, above this limit UV radiation is strongly absorbed by neutral hydrogen, since photons at these energies are able to ionise hydrogen, which has a much higher cross sectional area $\sigma_{\rm H}$ ($\sim 10^{-17}$cm^2 at 1 Ryd) than the dust. Neutral helium can also significantly attenuate the UV radiation at energies above 24.6 eV.

To illustrate how different components impact the spectrum at different energies, we show in figure 1 the Black (1987) interstellar radiation field and the resulting spectrum after it has passed through a total hydrogen column density $N_{\rm H_{tot}} = 1.6 \times 10^{21}\,{\rm cm}^{-2}$ at solar metallicity, including an HI column density $N_{\rm HI} = 1.2 \times 10^{20}\,{\rm cm}^{-2}$ and a HeI column density $N_{\rm HeI} = 1.6 \times 10^{20}\,{\rm cm}^{-2}$, as calculated by CLOUDY. We then compare these to a spectrum attenuated by only HI, by HI and HeI, and by HI, HeI and dust, calculated using the frequency dependent cross sections of Verner et al. (1996) and the dust opacities from Martin & Whittet (1990). We see that at energies just below 1 Ryd the UV radiation is suppressed by dust absorption, while the strong break above 1 Ryd is caused by neutral hydrogen. Comparing the green curve to the blue and yellow curves, we also see that absorp-

tion by neutral helium is important at higher energies, from a few Rydbergs up to 100 Ryd, while dust absorption is relatively unimportant at these higher energies. Note that the attenuated spectrum calculated by CLOUDY (the red curve) includes thermal emission from dust grains, which is why it is slightly higher than the incident spectrum at low energies $E < 10^{-4}$ Ryd.

While the column densities considered in the above example are typical of cold, atomic interstellar gas, there are certain regimes in which we also need to include the attenuation by additional species. For example, once the gas becomes molecular, the H_2 column density can be greater than the neutral hydrogen column density. Furthermore, at the high temperatures and low densities that are typical of the circumgalactic medium (for example $T \sim 10^5$ K, $n_{\rm H_{tot}} \sim 10^{-4}\,{\rm cm^{-3}}$), helium is singly ionised and shielding of radiation above 54.4 eV by HeII can be important. Therefore, to calculate the shielded photoionisation rates of species with ionisation energies above 13.6 eV, we need to account for the attenuation by four species: HI, H_2, HeI and HeII. For an incident spectrum with intensity J_ν per unit solid angle per unit frequency, the photoionisation rate of species i, $\Gamma_{i,\rm thick}$, is then given by:

$$\Gamma_{i,\rm thick} = \int_{\nu_{0,i}}^{\infty} \frac{4\pi J_\nu}{h\nu} \exp(-N_{\rm HI}\sigma_{\nu,\rm HI} - N_{\rm H_2}\sigma_{\nu,\rm H_2} - N_{\rm HeI}\sigma_{\nu,\rm HeI} - N_{\rm HeII}\sigma_{\nu,\rm HeII})\sigma_{\nu,i} d\nu\,, \quad (3.5)$$

where $\sigma_{\nu,i}$ and $\nu_{0,i}$ are respectively the frequency dependent cross section and the ionisation threshold frequency of species i.

Calculating these integrals at every timestep in the chemistry solver would be too computationally expensive, so instead we need to pre-compute them and tabulate the results. However, this would require us to tabulate the optically thick rates in four dimensions, one for each of the attenuating column densities, for every species. Such tables would require too much memory to be feasible. To reduce the size of the tables, we note that the H_2 cross section can be approximated as:

$$\sigma_{\nu,\rm H_2} \approx \begin{cases} 3.00\sigma_{\nu,\rm HI} & h\nu > 15.4\,{\rm eV} = h\nu_{0,\rm H_2} \\ 0 & \text{otherwise.} \end{cases} \quad (3.6)$$

Similarly, the HeII cross section can be approximated as:

$$\sigma_{\nu,\rm HeII} \approx \begin{cases} 0.75\sigma_{\nu,\rm HeI} & h\nu > 54.4\,{\rm eV} = h\nu_{0,\rm HeII} \\ 0 & \text{otherwise.} \end{cases} \quad (3.7)$$

Using these approximations, we can divide the shielded photoionisation rates into three integrals as follows:

$$\begin{aligned}\Gamma_{i,\rm thick} = &\int_{\nu_{0,i}}^{\nu_{0,\rm H_2}} \frac{4\pi J_\nu}{h\nu} \exp(-N_{\rm HI}\sigma_{\nu,\rm HI})\sigma_{\nu,i} d\nu + \\ &\int_{\nu_{0,\rm H_2}}^{\nu_{0,\rm HeII}} \frac{4\pi J_\nu}{h\nu} \exp(-N_{\rm H}^{\rm eff}\sigma_{\nu,\rm HI} - N_{\rm HeI}\sigma_{\nu,\rm HeI})\sigma_{\nu,i} d\nu + \\ &\int_{\nu_{0,\rm HeII}}^{\infty} \frac{4\pi J_\nu}{h\nu} \exp(-N_{\rm H}^{\rm eff}\sigma_{\nu,\rm HI} - N_{\rm He}^{\rm eff}\sigma_{\nu,\rm HeI})\sigma_{\nu,i} d\nu \\ &= \Gamma_{i,\rm thin}(S^i_{\rm gas,1}(N_{\rm HI}) + S^i_{\rm gas,2}(N_{\rm H}^{\rm eff}, N_{\rm HeI}) \\ &+ S^i_{\rm gas,3}(N_{\rm H}^{\rm eff}, N_{\rm He}^{\rm eff})), \end{aligned} \quad (3.8)$$

where the effective hydrogen and helium column densities are:

$$N_{\rm H}^{\rm eff} = N_{\rm HI} + 3.00 N_{\rm H_2} \quad (3.9)$$

$$N_{\rm He}^{\rm eff} = N_{\rm HeI} + 0.75 N_{\rm HeII}. \quad (3.10)$$

These effective column densities also account for the attenuation by H_2 and HeII respectively. Note that equation 3.8 is valid for species with an ionisation threshold frequency $\nu_{0,i} < \nu_{0,\rm H_2}$. If $\nu_{0,i} \geqslant \nu_{0,\rm H_2}$, the first integral will be zero. Similarly, the second integral in equation 3.8 will also be zero if $\nu_{0,i} \geqslant \nu_{0,\rm HeII}$.

By using these approximations, we only need to create tables of $S_{\rm gas,\{1,2,3\}}$ in up to two dimensions, which greatly reduces the memory that they require. This approach is not exact, but we find that it introduces errors in $\Gamma_{i,\rm thick}$ of at most a few tens of per cent, and typically much less than this. In appendix A we show the relative errors in the photoionisation rates of each species that are introduced by these approximations. For each species i we use equation 3.8 to tabulate the integrals $S^i_{\rm gas,1}(N_{\rm HI})$, $S^i_{\rm gas,2}(N_{\rm H}^{\rm eff}, N_{\rm HeI})$ and $S^i_{\rm gas,3}(N_{\rm H}^{\rm eff}, N_{\rm He}^{\rm eff})$ as a function of the given column densities from 10^{15} to 10^{24} cm^{-2} in intervals of 0.1 dex. Added together, these integrals give the ratio of the optically thick to the optically thin photoionisation rate of species i, $S^i_{\rm gas}(N_{\rm HI}, N_{\rm H_2}, N_{\rm HeI}, N_{\rm HeII})$.

3.2 Photodissociation

The photodissociation rates of molecular species are attenuated by dust according to equation 3.4, where we take the values of $\gamma^i_{\rm d}$ calculated for the Draine (1978) interstellar radiation field from table 2 of van Dishoeck et al. (2006) where available, or from table B2 of Glover et al. (2010) otherwise. In addition to dust shielding, the absorption of Lyman Werner radiation (i.e. photon energies $11.2\,{\rm eV} < h\nu < 13.6\,{\rm eV}$) by molecular hydrogen allows H_2 to become self-shielded. An accurate treatment of this effect would require us to solve the radiative transfer of the Lyman Werner radiation and to follow the level populations of the rovibrational states of the H_2 molecule, which would be computationally expensive. However, we can approximate the self-shielding of H_2 as a function of H_2 column density. For example, the following analytic fitting function from Draine & Bertoldi (1996) is commonly used in hydrodynamic simulations of galaxies and molecular clouds (e.g. Glover & Jappsen 2007; Glover et al. 2010; Gnedin et al. 2009; Christensen et al. 2012; Krumholz 2012):

$$S^{\rm H_2}_{\rm self} = \frac{1-\omega_{\rm H_2}}{(1+x/b_5)^\alpha} + \frac{\omega_{\rm H_2}}{(1+x)^{1/2}} \exp(-8.5\times10^{-4}(1+x)^{1/2}), \quad (3.11)$$

where $x \equiv N_{\rm H_2}/(5\times10^{14}{\rm cm^{-2}})$, $\omega_{\rm H_2}$ and α are adjustable parameters (Draine & Bertoldi 1996 use $\omega_{\rm H_2} = 0.035$ and $\alpha = 2$), $b_5 \equiv b/(10^5{\rm cm\ s^{-1}})$ and b is the Doppler broadening parameter. This function was introduced by Draine & Bertoldi (1996) and was motivated by their detailed radiative transfer and photodissociation calculations. The suppression factor $S^{\rm H_2}_{\rm self}$ initially declines rapidly (indicating increased shielding) with $N_{\rm H_2}$ as individual Lyman Werner lines shield themselves. However, once these lines become

saturated, the shielding is determined by the wings of the lines, leading to a shallow power law dependence $\sim N_{\rm H_2}^{-1/2}$. Finally, at high column densities the lines overlap, creating an exponential cut off in the self-shielding function.

Some authors have used equation 3.11 with different values for some of the parameters. For example, Gnedin et al. (2009) and Christensen et al. (2012) adopt a value $\omega_{\rm H_2} = 0.2$, as this gives better agreement between their model for H_2 formation and observations of atomic and molecular gas fractions in nearby galaxies.

Wolcott-Green et al. (2011) also investigate the validity of equation 3.11 and compare it to their detailed radiative transfer calculations of Lyman Werner radiation through simulated haloes at high redshift ($z \sim 10$). They find that equation 3.11, with $\omega_{\rm H_2} = 0.035$ and $\alpha = 2$, as used by Draine & Bertoldi (1996), underestimates the value of $S_{\rm self}^{\rm H_2}$ (i.e. it predicts too strong self-shielding) by up to an order of magnitude in warm gas (with $T \gtrsim 500$ K). They argue that this discrepancy arises because the assumptions made in Draine & Bertoldi (1996) are only accurate for cold gas in which only the lowest rotational states of H_2 are populated. However, they obtain better agreement with their calculations (within ~ 15 per cent) if they use equation 3.11 with $\alpha = 1.1$.

We have compared the H_2 self-shielding function of Draine & Bertoldi (1996) and the modification to this function suggested by Wolcott-Green et al. (2011), with $\alpha = 1.1$, to the ratio of the optically thick to optically thin H_2 photodissociation rates predicted by Cloudy in primordial gas. Details of this comparison can be found in appendix B. We find that neither function produces satisfactory agreement with Cloudy. For example, both overestimate $S_{\rm self}^{\rm H_2}$ compared to Cloudy by a factor ~ 3 at H_2 column densities $N_{\rm H_2} \gtrsim 10^{17}\,{\rm cm}^{-2}$ in gas with a temperature $T = 100$ K (see figure B1). We also find that the temperature dependence of $S_{\rm self}^{\rm H_2}$ predicted by Cloudy is not accurately reproduced by the modified self-shielding function from Wolcott-Green et al. (2011). Furthermore, Wolcott-Green et al. (2011) only consider gas in which the Doppler broadening is purely thermal. However, if it is dominated by turbulence then equation 3.11 will be independent of temperature.

To obtain a better fit to the H_2 self-shielding predicted by Cloudy (with its 'big H2' model), we modified equation 3.11 as follows:

$$S_{\rm self}^{\rm H_2} = \frac{1-\omega_{\rm H_2}(T)}{(1+x'/b_5)^{\alpha(T)}} \exp(-5\times10^{-7}(1+x')) + \frac{\omega_{\rm H_2}(T)}{(1+x')^{1/2}} \exp(-8.5\times10^{-4}(1+x')^{1/2}), \quad (3.12)$$

where $x' = N_{\rm H_2}/N_{\rm crit}(T)$. To reproduce the temperature dependence of $S_{\rm self}^{\rm H_2}$ that we see in Cloudy, we fit the parameters $\omega_{\rm H_2}(T)$, $\alpha(T)$ and $N_{\rm crit}(T)$ as functions of the temperature T. We obtain the best agreement with Cloudy using:

$$\omega_{\rm H_2}(T) = 0.013\left[1+\left(\frac{T}{2700\,{\rm K}}\right)^{1.3}\right]^{\frac{1}{1.3}} \exp\left[-\left(\frac{T}{3900\,{\rm K}}\right)^{14.6}\right], \quad (3.13)$$

$$\alpha(T) = \begin{cases} 1.4 & T < 3000\,{\rm K} \\ \left(\frac{T}{4500\,{\rm K}}\right)^{-0.8} & 3000\leqslant T < 4000\,{\rm K} \\ 1.1 & T \geqslant 4000\,{\rm K}, \end{cases} \quad (3.14)$$

$$\frac{N_{\rm crit}(T)}{10^{14}{\rm cm}^{-2}} = \begin{cases} 1.3\left[1+\left(\frac{T}{600\,{\rm K}}\right)^{0.8}\right] & T < 3000\,{\rm K} \\ \left(\frac{T}{4760\,{\rm K}}\right)^{-3.8} & 3000\leqslant T < 4000\,{\rm K} \\ 2.0 & T \geqslant 4000\,{\rm K}. \end{cases} \quad (3.15)$$

The H_2 self-shielding factor that we obtain with equations 3.12 to 3.15 agrees with Cloudy to within 30 per cent at 100 K for $N_{\rm H_2} < 10^{21}\,{\rm cm}^{-2}$, and to within 60 per cent at 5000 K for $N_{\rm H_2} < 10^{20}\,{\rm cm}^{-2}$ (see appendix B).

Doppler broadening of the Lyman Werner lines suppresses self-shielding. In a hydrodynamic simulation there are a number of ways we can estimate b (see Glover & Jappsen (2007) for a more detailed discussion of some of the approximations that have been used in the literature). In this paper we shall include turbulence with a constant velocity dispersion of 5 km s^{-1} (unless stated otherwise), which corresponds to a turbulent Doppler broadening parameter of $b_{\rm turb} = 7.1\,{\rm km\,s}^{-1}$, as used by Krumholz (2012). We also include thermal Doppler broadening $b_{\rm therm}$, which is related to the temperature T by:

$$b_{\rm therm} = \sqrt{\frac{2k_BT}{m_{\rm H_2}}}, \quad (3.16)$$

where $m_{\rm H_2}$ is the mass of an H_2 molecule. The total Doppler broadening parameter is then:

$$b = \sqrt{b_{\rm therm}^2 + b_{\rm turb}^2}. \quad (3.17)$$

CO has a dissociation energy of 11.1 eV, which is very close to the lower energy of the Lyman Werner band. Therefore, photons in the Lyman Werner band are also able to dissociate CO. CO is photodissociated via absorptions in discrete lines (dissociation via continuum absorption is negligible for CO), so it can become self-shielded once these lines are saturated, but it can also be shielded by H_2, as its lines also lie in the Lyman Werner band. The shielding factor of CO due to H_2 and CO ($S_{\rm self,H_2}^{\rm CO}$) has been tabulated in two dimensions as a function of $N_{\rm H_2}$ and $N_{\rm CO}$ by Visser et al. (2009) for different values of the Doppler broadening and excitation temperatures of CO and H_2. High resolution versions of these tables can be found on their website[6]. We use their table calculated for Doppler widths of CO and H_2 of $0.3\,{\rm km\,s}^{-1}$ and $3.0\,{\rm km\,s}^{-1}$ respectively, and excitation temperatures of CO and H_2 of 50.0 K and 353.6 K respectively, with the elemental isotope ratios of Carbon and Oxygen from Wilson (1999) for the local ISM.

Additionally, dust can shield CO, where the dust shielding factor is given by equation 3.4 (with $\gamma_{\rm d}^{\rm CO} = 3.53$).

To summarise, the optically thick photodissociation rates of H_2 and CO are:

[6] `home.strw.leidenuniv.nl/~ewine/photo`

$$\Gamma_{\mathrm{H_2,thick}} = \Gamma_{\mathrm{H_2,thin}} S_{\mathrm{d}}^{\mathrm{H_2}}(N_{\mathrm{H_{tot}}}, Z) S_{\mathrm{self}}^{\mathrm{H_2}}(N_{\mathrm{H_2}}) \quad (3.18)$$

$$\Gamma_{\mathrm{CO,thick}} = \Gamma_{\mathrm{CO,thin}} S_{\mathrm{d}}^{\mathrm{CO}}(N_{\mathrm{H_{tot}}}, Z) S_{\mathrm{self,H_2}}^{\mathrm{CO}}(N_{\mathrm{CO}}, N_{\mathrm{H_2}}), \quad (3.19)$$

while the photoionisation and photodissociation rates of the remaining species are:

$$\Gamma_{i,\mathrm{thick}} = \Gamma_i S^i, \quad (3.20)$$

where $S^i = S_{\mathrm{d}}^i(N_{\mathrm{H_{tot}}}, Z)$ if the ionisation energy is below 13.6 eV, or $S_{\mathrm{gas}}^i(N_{\mathrm{HI}}, N_{\mathrm{H_2}}, N_{\mathrm{HeI}}, N_{\mathrm{HeII}})$ otherwise.

To calculate the optically thick rates, we thus need to specify the column densities of HI, HeI, HeII, H_2, H_{tot} and CO, and the metallicity.

3.3 Photoheating

The photoheating rate of a species is the photoionisation rate Γ_i multiplied by the average excess energy of the ionising photons $\langle\epsilon_i\rangle$ (see equations 3.5 and 3.6 from paper I). As the gas becomes shielded, the shape of the UV spectrum changes, as more energetic photons are able to penetrate deeper into the gas, thus $\langle\epsilon_i\rangle$ increases. In particular, species that have an ionisation energy above 13.6 eV may be strongly affected by absorption by HI, H_2, HeI and HeII (see section 3.1). For UV radiation attenuated by column densities N_{HI}, $N_{\mathrm{H_2}}$, N_{HeI} and N_{HeII}, the average excess energy of ionising photons for species i is:

$$\begin{aligned}
&\langle\epsilon_{i,\mathrm{thick}}\rangle = \\
&\left[\int_{\nu_{0,i}}^{\infty} \frac{4\pi J_\nu}{h\nu} \exp(-N_{\mathrm{HI}}\sigma_{\nu,\mathrm{HI}} - N_{\mathrm{H_2}}\sigma_{\nu,\mathrm{H_2}} - N_{\mathrm{HeI}}\sigma_{\nu,\mathrm{HeI}} \right. \\
&\left. - N_{\mathrm{HeII}}\sigma_{\nu,\mathrm{HeII}})(h\nu - h\nu_{0,i})\sigma_{\nu,i} d\nu\right] \Bigg/ \\
&\left[\int_{\nu_{0,i}}^{\infty} \frac{4\pi J_\nu}{h\nu} \exp(-N_{\mathrm{HI}}\sigma_{\nu,\mathrm{HI}} - N_{\mathrm{H_2}}\sigma_{\nu,\mathrm{H_2}} - N_{\mathrm{HeI}}\sigma_{\nu,\mathrm{HeI}} \right. \\
&\left. - N_{\mathrm{HeII}}\sigma_{\nu,\mathrm{HeII}})\sigma_{\nu,i} d\nu\right]. \quad (3.21)
\end{aligned}$$

To pre-compute these integrals, we would require four dimensional tables. However, as described in section 3.1, we can use the approximations in equations 3.6 and 3.7 to reduce the size of these tables. With these approximations, equation 3.21 becomes:

$$\begin{aligned}
&\langle\epsilon_{i,\mathrm{thick}}\rangle = \\
&\left[\int_{\nu_{0,i}}^{\nu_{0,\mathrm{H_2}}} \frac{4\pi J_\nu}{h\nu} \exp(-N_{\mathrm{HI}}\sigma_{\nu,\mathrm{HI}})(h\nu - h\nu_{0,i})\sigma_{\nu,i} d\nu + \right. \\
&\int_{\nu_{0,\mathrm{H_2}}}^{\nu_{0,\mathrm{HeII}}} \frac{4\pi J_\nu}{h\nu} \exp(-N_{\mathrm{H}}^{\mathrm{eff}}\sigma_{\nu,\mathrm{HI}} \\
&-N_{\mathrm{HeI}}\sigma_{\nu,\mathrm{HeI}})(h\nu - h\nu_{0,i})\sigma_{\nu,i} d\nu + \\
&\int_{\nu_{0,\mathrm{HeII}}}^{\infty} \frac{4\pi J_\nu}{h\nu} \exp(-N_{\mathrm{H}}^{\mathrm{eff}}\sigma_{\nu,\mathrm{HI}} \\
&\left. -N_{\mathrm{He}}^{\mathrm{eff}}\sigma_{\nu,\mathrm{HeI}})(h\nu - h\nu_{0,i})\sigma_{\nu,i} d\nu\right] \Bigg/ \\
&\left[\int_{\nu_{0,i}}^{\nu_{0,\mathrm{H_2}}} \frac{4\pi J_\nu}{h\nu} \exp(-N_{\mathrm{HI}}\sigma_{\nu,\mathrm{HI}})\sigma_{\nu,i} d\nu + \right. \\
&\int_{\nu_{0,\mathrm{H_2}}}^{\nu_{0,\mathrm{HeII}}} \frac{4\pi J_\nu}{h\nu} \exp(-N_{\mathrm{H}}^{\mathrm{eff}}\sigma_{\nu,\mathrm{HI}} - N_{\mathrm{HeI}}\sigma_{\nu,\mathrm{HeI}})\sigma_{\nu,i} d\nu + \\
&\left. \int_{\nu_{0,\mathrm{HeII}}}^{\infty} \frac{4\pi J_\nu}{h\nu} \exp(-N_{\mathrm{H}}^{\mathrm{eff}}\sigma_{\nu,\mathrm{HI}} - N_{\mathrm{He}}^{\mathrm{eff}}\sigma_{\nu,\mathrm{HeI}})\sigma_{\nu,i} d\nu\right], \quad (3.22)
\end{aligned}$$

where the effective hydrogen and helium column densities, $N_{\mathrm{H}}^{\mathrm{eff}}$ and $N_{\mathrm{He}}^{\mathrm{eff}}$, are given in equations 3.9 and 3.10, and account for the attenuation by H_2 and HeII respectively.

For each species with an ionisation energy above 13.6 eV, we tabulate the six integrals in equation 3.22 as a function of the given column densities from 10^{15} to 10^{24} cm^{-2} in intervals of 0.1 dex.

4 CHEMISTRY AND COOLING IN SHIELDED GAS

In this section we look at gas that is illuminated by a radiation field that is attenuated by some column density. We consider a one-dimensional plane-parallel slab of gas with solar metallicity that is illuminated from one side by the Black (1987) interstellar radiation field. The slab is divided into cells such that the total hydrogen column density from the illuminated face of the slab increases from 10^{14} cm^{-2} to 10^{24} cm^{-2} in increments of 0.01 dex. Using the methods described in section 3, we then use the resulting column densities to calculate the attenuated photoionisation, photodissociation and photoheating rates and hence to solve for the chemical and thermal evolution in each cell.

The thermo-chemical evolution of a cell will depend on the chemical state of all cells between it and the illuminated face of the slab, since HI, HeI, HeII, H_2 and CO contribute to the shielding of certain species. We therefore integrate the thermo-chemistry over a timestep that is determined such that the relative change in the column densities of HI, HeI, HeII, H_2 and CO in each cell will be below some tolerance ϵ (which we take to be 0.1), as estimated based on their change over the previous timestep. In other words, the timestep Δt is given by:

$$\Delta t = \min\left(\frac{\epsilon N_i \Delta t^{\mathrm{prev}}}{\Delta N_i^{\mathrm{prev}} + \psi}\right), \quad (4.1)$$

where N_i is the column density of species i and $\Delta N_i^{\mathrm{prev}}$ is the

change in N_i over the previous timestep $\Delta t^{\rm prev}$. We take the minimum over the five species that contribute to shielding and over all gas cells. ψ is a small number that is introduced to prevent division by zero - we take $\psi = 10^{-40}$. At the end of each timestep we then update the column densities of these five species for each cell.

4.1 Comparison with Cloudy

We use Cloudy version 13.01 to calculate the abundances and the cooling and heating rates in chemical equilibrium as a function of the total hydrogen column density, $N_{\rm H_{tot}}$, and compare them to the results from our model. These were calculated for a number of temperatures and densities, which were held fixed across the entire gas slab for this comparison. We add turbulence to the Cloudy models with a Doppler broadening parameter $b_{\rm turb} = 7.1\,{\rm km\,s^{-1}}$, in agreement with the default value that we use.

Cloudy has two possible models for the microphysics of molecular hydrogen. Their 'big H2' model follows the level populations of 1893 rovibrational states of molecular hydrogen, and the photodissociation rates from the various electronic and rovibrational transitions via the Solomon process are calculated self-consistently. However, as this is computationally expensive, Cloudy also has a 'small H2' model in which the ground electronic state of molecular hydrogen is split between two vibrational states, a ground state and a single vibrationally excited state, following the approach of Tielens & Hollenbach (1985). These two states are then treated as separate species in the chemical network. The photodissociation rates of H_2 in the small H2 model are taken from Elwert et al. (2005) by default (although there are options to use alternative dissociation rates). We primarily focus on the big H2 model for this comparison, as it includes a more complete treatment of the microphysics involved, although we also show the molecular abundances from the small H2 model to illustrate the differences between these two Cloudy models.

The comparison with Cloudy is shown in figure 2 for gas at solar metallicity with a constant density $n_{\rm H} = 100\,{\rm cm^{-3}}$ and a temperature $T = 300$ K. More examples at other densities and temperatures can be found on our website[7]. In the top two panels we compare some of the equilibrium molecular and ionisation fractions. Compared to the big H2 model in Cloudy, the HI-H_2 transition occurs at a somewhat lower column density in our model, with a molecular hydrogen fraction $x_{\rm H_2} = 0.5$ at $N_{\rm H_{tot}} \approx 8.1\times10^{19}\,{\rm cm^{-2}}$, compared to $N_{\rm H_{tot}} \approx 2.8\times10^{20}\,{\rm cm^{-2}}$ in Cloudy. Below this transition the molecular hydrogen fraction tends towards a value $x_{\rm H_2} \approx 5\times10^{-5}$ in our model. This fraction is sufficiently high for the H_2 to shield itself from the Lyman Werner radiation before dust shielding becomes important (with $S_{\rm d}^{\rm H_2} \sim 0.1$ at $A_v \approx 0.6$), as the self-shielding is significant at relatively low H_2 column densities (with $S_{\rm self}^{\rm H_2} \sim 0.1$ at $N_{\rm H_2} \approx 6\times10^{15}\,{\rm cm^{-2}}$, as defined in equation 3.12). The H_2 fraction in the photodissociated region is $x_{\rm H_2} \approx 3\times10^{-5}$ for Cloudy's big H2 model, which is slightly lower than in our model. This explains why the gas becomes self-shielded at a somewhat higher total column density in Cloudy than in our model. This discrepancy occurs because we use a different photodissociation rate. As discussed in paper I, the dissociation rate of H_2 via the Solomon process depends on the level populations of the rovibrational states of H_2. This is calculated self-consistently in the big H2 model of Cloudy, whereas we must use an approximation to the photodissociation rate, as we do not follow the rovibrational levels of H_2. We therefore miss, for example, the dependence of the photodissociation rate on density, which affects the rovibrational level populations.

For comparison, we also show the molecular hydrogen abundance predicted by the small H2 model of Cloudy in the top panel of figure 2 *(black dot-dot-dashed line)*. The HI-H_2 transition in the small H2 model is closer to our model than the big H2 model, with $x_{\rm H_2} = 0.5$ at $N_{\rm H_{tot}} \approx 1.1\times10^{20}\,{\rm cm^{-2}}$. However, the transition in our model is somewhat steeper than in Cloudy's small H2 model.

While the HI-H_2 transition in this example, with constant temperature and density, is caused by H_2 self-shielding, we would not expect temperatures as low as 300 K in the photodissociated region, nor would we expect densities as high as 100 ${\rm cm^{-3}}$. This example therefore overestimates the importance of H_2 self-shielding. In section 4.3 we address this issue by considering a cloud that is in thermal and pressure equilibrium.

After the HI-H_2 transition the neutral hydrogen abundance $x_{\rm HI}$ tends to $x_{\rm HI} \approx 0.01$ at $N_{\rm H_{tot}} \gtrsim 10^{22}\,{\rm cm^{-2}}$ in our model, compared to $x_{\rm HI} \approx 0.05$ in Cloudy. This difference arises because the cosmic ray dissociation rate af H_2 that we use in our model, which is based on the rates in the UMIST database, is an order of magnitude lower than that used in Cloudy.

The onset of the HI-H_2 transition leads to a rise in the CO abundance, although most carbon is still in CII at this transition. At higher column densities the dust is able to shield the photodissociation of CO, which becomes fully shielded at $N_{\rm H_{tot}} \gtrsim 10^{22}\,{\rm cm^{-2}}$. This second transition also corresponds to a drop in the abundances of singly ionised metals with ionisation energies lower than 1 Ryd, such as CII and SiII, whose photoionisation rates are attenuated by dust rather than by neutral hydrogen and helium. These species become shielded at a slightly higher column density in our model than in Cloudy (for example, CII has an ionisation fraction $x_{\rm CII} = 0.1$ at $N_{\rm H_{tot}} \approx 7\times10^{21}\,{\rm cm^{-2}}$ in our model, compared to $N_{\rm H_{tot}} \approx 4\times10^{21}\,{\rm cm^{-2}}$ in Cloudy).

In the bottom two panels of figure 2 we show the total cooling and heating rates for this example, along with the contributions from selected individual species. Before the HI-H_2 transition the cooling is dominated by SiII, FeII and CII, with heating coming primarily from photoionisation of neutral hydrogen. After this transition the photoheating rates drop rapidly, with the main heating mechanism being photoelectric dust heating, while the total cooling rates are lower and are primarily from molecular hydrogen. Once dust shielding begins to significantly attenuate the UV radiation field below 13.6 eV at a column density $N_{\rm H_{tot}} \sim 10^{21}\,{\rm cm^{-2}}$, the photoelectric heating rate falls sharply. For $N_{\rm H_{tot}} \gtrsim 10^{22}\,{\rm cm^{-2}}$ the heating rates are dominated by cosmic rays. In our model this is primarily from cosmic ray ionisation heating of H_2. However, Cloudy only includes cosmic ray heating of HI, hence the total heating

[7] `http://noneqism.strw.leidenuniv.nl`

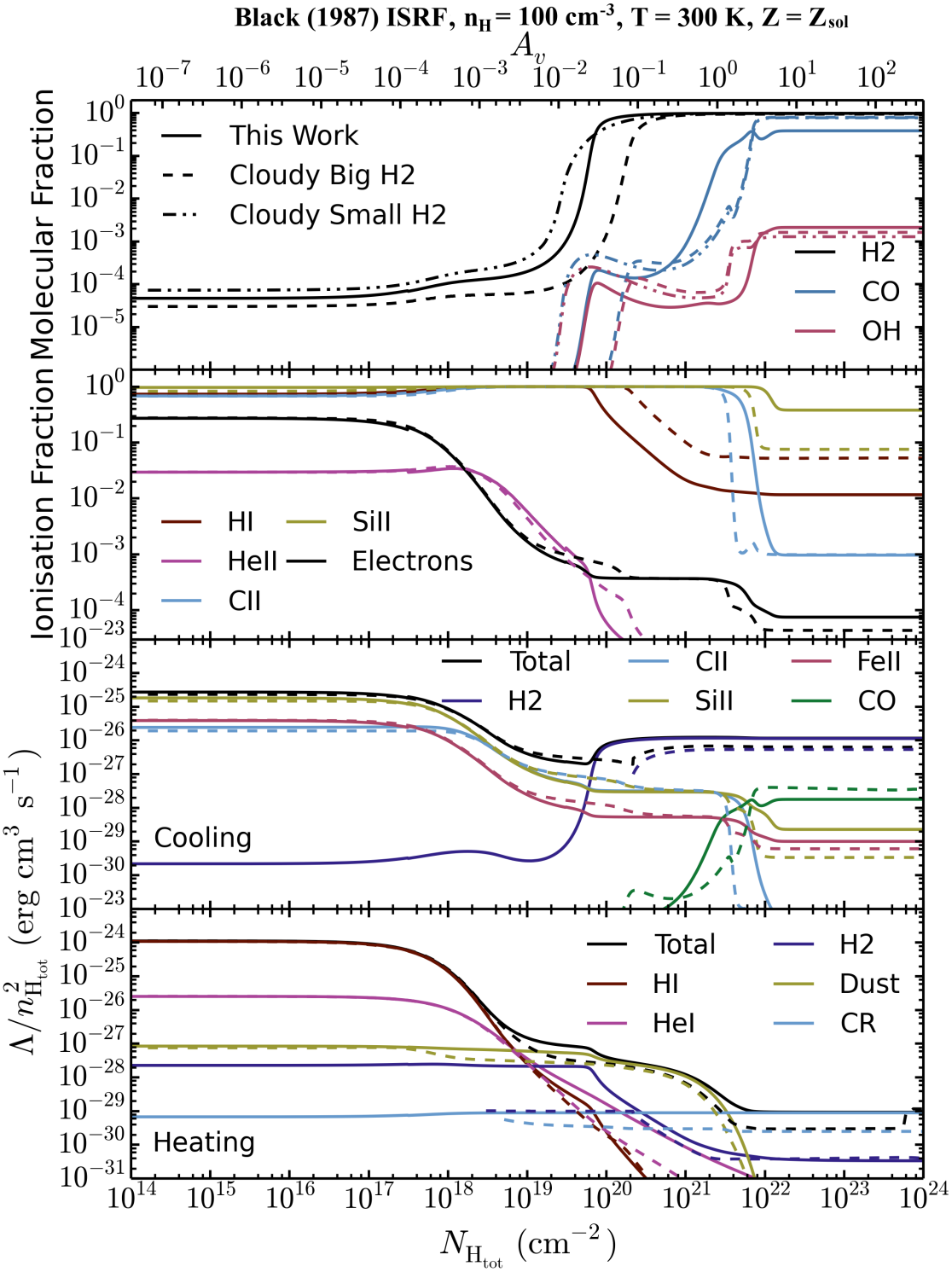

Figure 2. Chemistry and cooling properties of a one-dimensional plane-parallel slab of gas illuminated by the Black (1987) interstellar radiation field, plotted as a function of the total hydrogen column density into the gas cloud, assuming solar metallicity with constant density $n_{\rm H} = 100\,{\rm cm}^{-3}$ and constant temperature $T = 300$ K. The corresponding dust extinction is marked on the top x-axis, where we have used $A_v/N_{\rm H_{tot}} = 4 \times 10^{-22}\,{\rm mag\,cm^2}$ for a solar metallicity gas (see section 3.1). We compare our model *(solid lines)* to Cloudy using its big H2 model *(dashed lines)* and its small H2 model *(dot-dot-dashed lines; top panel only)* in chemical equilibrium. **Top panel:** equilibrium molecular fractions ($2n_{\rm H_2}/n_{\rm H_{tot}}$, $n_{\rm CO}/n_{\rm C_{tot}}$ and $n_{\rm OH}/n_{\rm O_{tot}}$); **second panel:** equilibrium ionisation fractions; **third panel:** equilibrium cooling rates; **bottom panel:** equilibrium heating rates. The small discontinuity in the electron abundance at $N_{\rm H_{tot}} \sim 3 \times 10^{17}\,{\rm cm}^{-2}$ is due to the recombination of hydrogen, which switches from case A to case B when the HI optical depth is unity.

rates in our model are higher than CLOUDY in this region. The most important coolants in the fully shielded gas are molecular hydrogen and CO.

We have also compared our abundances and cooling and heating rates with CLOUDY at densities of $1\,\mathrm{cm}^{-3}$ and $10^4\,\mathrm{cm}^{-3}$, and a temperature of 100 K. These results can be found on our website. We generally find good agreement with CLOUDY, although we sometimes find that the abundances of singly ionised metals with low ionisation energies, such as SiII and FeII, are in poor agreement in fully shielded gas, once carbon becomes fully molecular. This occurs at the highest densities that we consider, although we begin to see such discrepancies in the SiII abundance in figure 2. In this regime the ionisation of these species is typically dominated by charge transfer reactions between metal species, the rates of which tend to be uncertain. Moreover, a significant fraction of Si is found in SiO in the CLOUDY models and, because our simplified molecular network does not include silicon molecules, we are unable to reproduce the correct silicon abundances in fully shielded gas. Since the abundances of other low ionisation energy ions such as FeII and MgII are dependent on SiII due to charge transfer reactions in this regime, these species will also be uncertain in fully shielded gas. However, the predicted abundances of molecules such as H_2 and CO are in good agreement with CLOUDY in this regime.

4.2 Importance of turbulence for H_2 self-shielding

In the previous section we found that the small H_2 abundance in the photodissociated region can be sufficient to begin attenuating the photodissociation rate of molecular hydrogen via self-shielding before dust extinction becomes significant. However, the presence of turbulence in the gas can suppress self-shielding due to Doppler broadening of the Lyman Werner lines. In this section we investigate the impact that turbulence can have on the HI-H_2 transition by repeating the above calculations for three different values of the turbulent Doppler broadening parameter: $b_\mathrm{turb} = 0\,\mathrm{km\,s^{-1}}$, $b_\mathrm{turb} = 7.1\,\mathrm{km\,s^{-1}}$ (our default value) and $b_\mathrm{turb} = 14.2\,\mathrm{km\,s^{-1}}$. The thermal Doppler broadening parameter at 300 K is $b_\mathrm{therm} = 1.6\,\mathrm{km\,s^{-1}}$, thus the total Doppler broadening parameters are $b = 1.6\,\mathrm{km\,s^{-1}}$, $7.3\,\mathrm{km\,s^{-1}}$ and $14.3\,\mathrm{km\,s^{-1}}$.

In figure 3 we show the molecular and ionisation fractions for these three Doppler broadening parameters at a constant density $n_\mathrm{H_{tot}} = 100\,\mathrm{cm}^{-3}$ and a constant temperature $T = 300$ K. We find that, while the ion fractions are hardly affected, increasing the turbulent Doppler broadening parameter from 0 to 14.2 km s^{-1} increases the column density at which the hydrogen starts to become molecular by more than an order of magnitude, as it suppresses H_2 self-shielding. However, the transition also becomes sharper for higher values of b, so the change in the column density at which half of the hydrogen is molecular is less significant, increasing from $N_\mathrm{H_{tot}} \approx 3.3 \times 10^{19}\,\mathrm{cm}^{-2}$ to $N_\mathrm{H_{tot}} \approx 1.4 \times 10^{20}\,\mathrm{cm}^{-2}$. The transition to molecular hydrogen is still caused by H_2 self-shielding in these examples, even for the highest value of b that we consider here.

4.3 Atomic to molecular transition in thermal and pressure equilibrium

The previous sections considered gas at a constant temperature of 300 K, but figure 2 showed that the heating and cooling rates vary stongly with the column density into the cloud. Furthermore, we assumed a constant density throughout the cloud, which is unrealistic as gas at low column densities will be strongly photoheated and will thus typically have lower densities. It would therefore be more realistic to consider a cloud that is in thermal and pressure equilibrium. To achieve this, we first ran a series of models with different constant densities that were allowed to evolve to thermal equilibrium, from which we obtained the thermal equilibrium temperature on a two-dimensional grid of density and column density. Then, for each column density bin, we used this grid to determine the density that will give the assumed pressure. Finally, we imposed this isobaric density profile on the one-dimensional plane-parallel slab of gas and evolved it until it reached thermal and chemical equilibrium. This scenario is more typical of the two-phase ISM, in which gas is photoheated to higher temperatures, with lower densities, at low column densities, and then cools to a much colder and denser phase once the ionising photons have been attenuated and molecular cooling becomes important.

In figure 4 we show the results for a cloud with a constant pressure $P/k_\mathrm{B} = 10^3\,\mathrm{cm}^{-3}\,\mathrm{K}$, assuming solar metallicity. The equilibrium molecular and ionisation fractions of some species are shown in the top two panels of figure 4 as a function of the total column density $N_\mathrm{H_{tot}}$, the equilibrium gas temperature and density are shown in the middle panel, and the equilibrium cooling and heating rates are shown in the bottom two panels.

We see that gas is more strongly ionised in the photodissociated region compared to the constant temperature and density run in figure 2. This is due to both the higher temperature and the lower density. Furthermore, the molecular hydrogen fraction is much lower in this region, and the H_2 self-shielding is thus weaker. Hence, the HI-H_2 transition occurs at a higher column density compared to figure 2 ($x_{H_2} = 0.5$ at $N_\mathrm{H_{tot}} \approx 1.5 \times 10^{21}\,\mathrm{cm}^{-2}$ in figure 4, compared to $N_\mathrm{H_{tot}} \approx 8.1 \times 10^{19}\,\mathrm{cm}^{-2}$ in figure 2). The H_2 fraction first rises at $N_\mathrm{H_{tot}} \sim 2 \times 10^{20}\,\mathrm{cm}^{-2}$ due to a corresponding rise in the HI abundance, which is required to form H_2. The HI abundance increases because it is able to shield itself against ionising radiation above 1 Ryd (the HI column density here is $\sim 10^{17}\,\mathrm{cm}^{-2}$). However, the H_2 fraction still remains low after this initial increase ($x_{H_2} \approx 10^{-7}$). The HI-H_2 transition at $N_\mathrm{H_{tot}} \approx 1.5 \times 10^{21}\,\mathrm{cm}^{-2}$ is initially triggered by the increasing density, which enhances the formation rate of H_2 on dust grains with respect to the photodissociation rate. However, H_2 self-shielding then becomes significant and is responsible for the final transition to a fully molecular gas. When we repeat this model without H_2 self-shielding, we find that the HI-H_2 transition occurs at a factor ~ 5 higher column density, with $x_{H_2} = 0.5$ at $N_\mathrm{H_{tot}} \approx 7.2 \times 10^{21}\,\mathrm{cm}^{-2}$.

In figure 4, CO becomes fully shielded from dissociating radiation at $N_\mathrm{H_{tot}} \gtrsim 10^{22}\,\mathrm{cm}^{-2}$. Like in the constant density run in figure 2, this transition is determined by dust shielding.

Observations of diffuse clouds at low column densities find abundances of CH^+ that are several orders of magni-

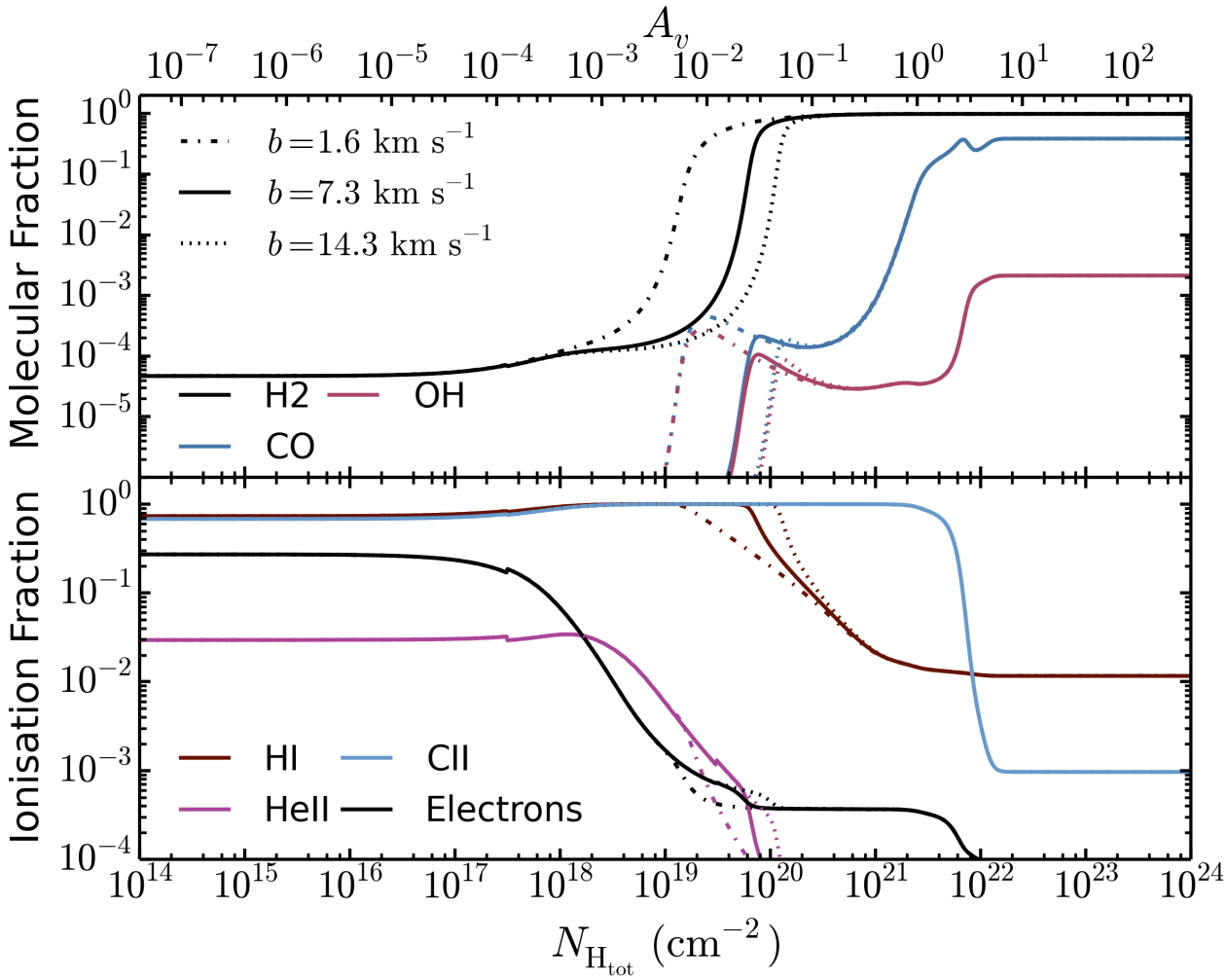

Figure 3. Comparison of the chemical properties of a one-dimensional plane-parallel slab of gas for three different Doppler broadening parameters, corresponding to different levels of turbulence in the gas, with $b = 1.6\,\mathrm{km\ s^{-1}}$ corresponding to pure thermal broadening. **Top panel:** equilibrium molecular fractions ($2n_{\mathrm{H_2}}/n_{\mathrm{H_{tot}}}$, $n_{\mathrm{CO}}/n_{\mathrm{C_{tot}}}$ and $n_{\mathrm{OH}}/n_{\mathrm{O_{tot}}}$); **bottom panel:** equilibrium ionisation fractions. These were calculated at solar metallicity, a constant density $n_{\mathrm{H}} = 100\,\mathrm{cm^{-3}}$ and a constant temperature $T = 300$ K. The strongest turbulence shown here ($b = 14.3\,\mathrm{km\ s^{-1}}$) increases the column density at which the hydrogen starts to become molecular by more than an order of magnitude compared to pure thermal Doppler broadening, although its impact on the transition column density at which $x_{\mathrm{H_2}} = 0.5$ is less significant.

tude higher than can be explained using standard chemical models (e.g. Federman et al. 1996; Sheffer et al. 2008; Visser et al. 2009). This also leads to predicted CO abundances that are lower than observed in such regions, as CH^+ is an important formation channel for CO. Various non-thermal production mechanisms for CH^+ have been proposed to alleviate this discrepancy. For example, Federman et al. (1996) suggest that Alfvén waves that enter the cloud can produce non-thermal motions between ions and neutral species, thus increasing the rates of ion-neutral reactions.

To see what effect such suprathermal chemistry has on our chemical network, we repeated the models in figures 2 and 4 with the kinetic temperature of all ion-neutral reactions replaced by an effective temperature that is enhanced by Alfvén waves, as given by the prescription of Federman et al. (1996) with an Alfvén speed of $3.3\,\mathrm{km\,s^{-1}}$. Following Sheffer et al. (2008) and Visser et al. (2009), we only include this enhancement of the ion-neutral reactions at low column densities, $N_{\mathrm{H_2}} < 4 \times 10^{20}\,\mathrm{cm^{-2}}$. In the model with a constant density $n_{\mathrm{H_{tot}}} = 100\,\mathrm{cm^{-3}}$ and constant temperature $T = 300\,\mathrm{K}$, we find that the CH^+ abundance is increased by up to four orders of magnitude at intermediate column densities $5 \times 10^{19}\,\mathrm{cm^{-2}} \lesssim \mathrm{N_{H_{tot}}} \lesssim 10^{21}\,\mathrm{cm^{-2}}$. The CO abundance is enhanced by up to a factor of 6 in this same region. We see similar enhancements in the model with a constant pressure $P/k_{\mathrm{B}} = 10^3\,\mathrm{cm^{-3}\,K}$, but only at column densities $10^{21}\,\mathrm{cm^{-2}} \lesssim \mathrm{N_{H_{tot}}} \lesssim 3 \times 10^{21}\,\mathrm{cm^{-2}}$, as the temperature at lower column densities is much higher than in the constant density model ($T > 1000\,\mathrm{K}$).

At low column densities the cooling rate in figure 4 is determined by several ionised species including SiII, FeII, FeIII and CII, along with NIII, OIII, NeIII and SIII (not shown in figure 4). Heating at low column densities is primarily from dust heating and photoionisation of HI and HeI. At $N_{\mathrm{H_{tot}}} \sim$

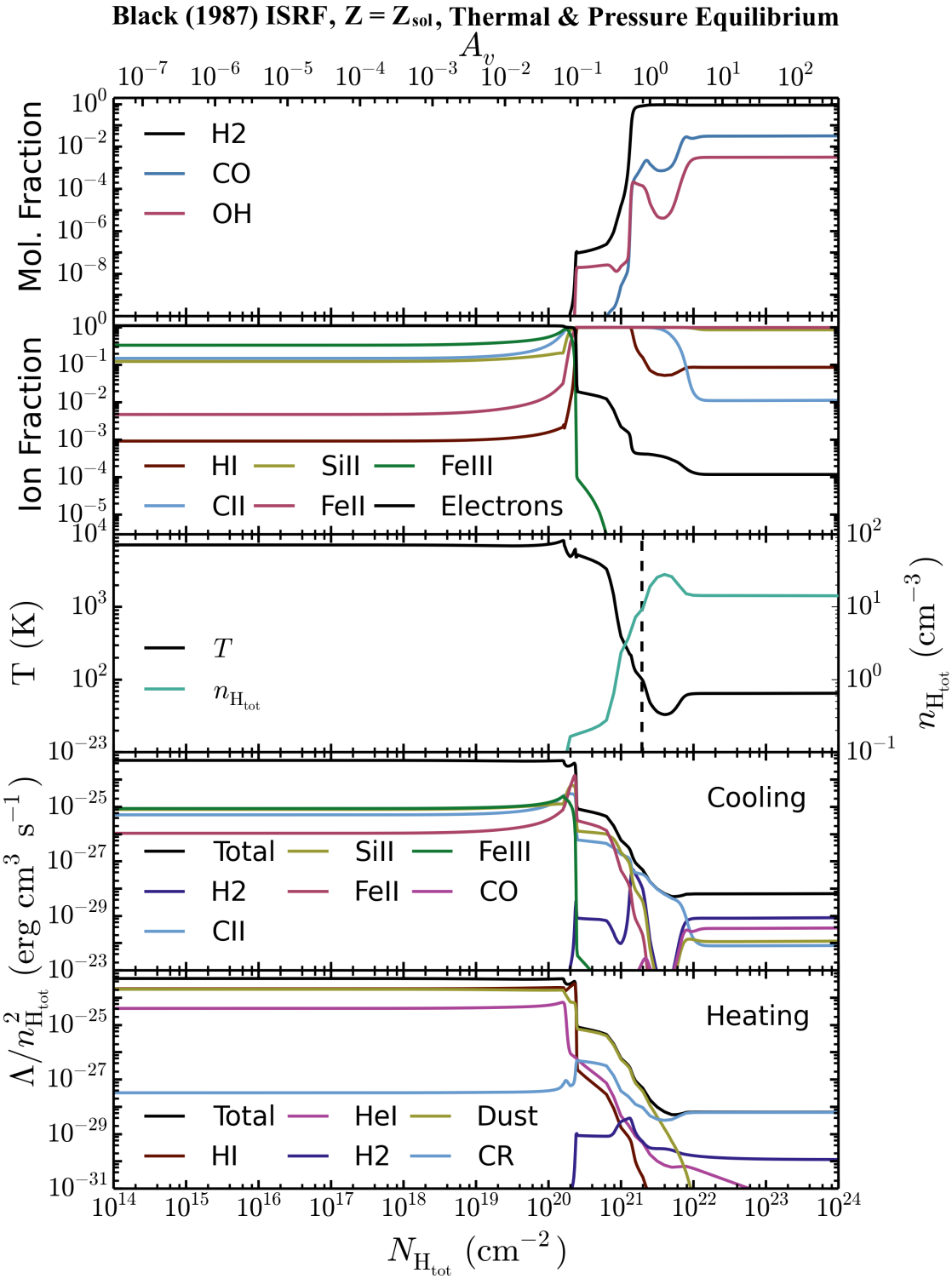

Figure 4. Chemistry and cooling properties of a one-dimensional plane-parallel slab of gas that is in thermal and pressure equilibrium with a pressure $P/k_B = 10^3\,\mathrm{cm}^{-3}\,\mathrm{K}$, plotted as a function of the total hydrogen column density into the gas cloud, assuming solar metallicity in the presence of the Black (1987) interstellar radiation field. **Top panel:** equilibrium molecular fractions ($2n_{H_2}/n_{H_{tot}}$, $n_{CO}/n_{C_{tot}}$ and $n_{OH}/n_{O_{tot}}$); **second panel:** equilibrium ionisation fractions; **third panel:** equilibrium gas temperature and density; **fourth panel:** equilibrium cooling rates; **bottom panel:** equilibrium heating rates. The vertical dashed line in the third panel indicates the column density at which the gas becomes Jeans unstable. To the right of this dashed line we would expect the gas cloud to become self-gravitating, and the density profile that we have imposed assuming pressure equilibrium will underestimate the typical densities corresponding to these column densities.

$2 \times 10^{20}\,\mathrm{cm}^{-2}$ the cooling rates from SiII and FeII peak as SiIII and FeIII recombine, creating a small dip in the temperature profile. The photoheating rate then drops sharply as the ionising radiation above 1 Ryd becomes shielded by HI, and the total heating rate becomes dominated by the dust photoelectric effect. The thermal equilibrium temperature reaches a minimum of 30 K at $N_{\mathrm{H_{tot}}} \sim 4 \times 10^{21}\,\mathrm{cm}^{-2}$ as the dust photoelectric heating becomes suppressed by dust shielding, leaving heating primarily from cosmic ray ionisation of H_2. However, after this point the carbon forms CO and the cooling becomes dominated by molecules (CO and H_2). These species are less efficient at cooling than CII, so the thermal equilibrium temperature increases to 60 K. Hence, the temperature in the fully molecular region is higher than the minimum at $N_{\mathrm{H_{tot}}} \sim 4 \times 10^{21}\,\mathrm{cm}^{-2}$.

We note that the assumption of pressure equilibrium in these examples will be unrealistic at high column densities, where the gas becomes self-gravitating. The vertical dashed line in the middle panel of figure 4 indicates the column density at which the size of the system, $N_{\mathrm{H_{tot}}}/n_{\mathrm{H_{tot}}}$, becomes larger than the local Jeans length, at $N_{\mathrm{H_{tot}}} \approx 2 \times 10^{21}\,\mathrm{cm}^{-2}$. Thus, we would expect the fully molecular region in these examples to have a higher density than we have used here.

We also considered a gas cloud with a pressure that is a factor 100 larger than is shown in figure 4. This results in higher densities in the fully shielded region that are more typical of molecular clouds ($n_{\mathrm{H_{tot}}} \sim 10^3\,\mathrm{cm}^{-3}$), although the densities in the photodissociated region are then higher than we would expect for the warm ISM. The cumulative H_2 fractions for the two pressures are shown in figures 5 and 6 with and without H_2 self-shielding respectively (see section 5). The top panels in these figures are at the lower pressure ($P/k_{\mathrm{B}} = 10^3\,\mathrm{cm}^{-3}\,\mathrm{K}$), and the bottom panels are at the higher pressure ($P/k_{\mathrm{B}} = 10^5\,\mathrm{cm}^{-3}\,\mathrm{K}$). In the left panels we use a metallicity $0.1Z_{\odot}$, and in the right panels we use solar metallicity. We find that in all of these examples H_2 self-shielding is again important for the final transition to fully molecular hydrogen, reducing the column density of this transition by up to two orders of magnitude compared to the same model without H_2 self-shielding.

We thus find that the effect of H_2 self-shielding can be weaker in a cloud that is in thermal and pressure equilibrium due to the lower densities at low column densities compared to a model with a constant density and temperature. However, H_2 self-shielding still determines the final transition to fully molecular hydrogen. Furthermore, H_2 self-shielding will be even more important if the pressure (and hence densities) are higher.

Figure 5 also demonstrates the dependence of the transition column density on pressure and metallicity. The HI-H_2 transition occurs at a lower column density for higher pressure and higher metallicity. Both of these trends are driven by H_2 self-shielding because the H_2 fraction in the dissociated region is higher at higher pressure (due to the increased density) and at higher metallicity (due to the increased formation of H_2 on dust grains, and also due to the increased cooling from metals, which results in a lower temperature and a higher density at a given pressure).

We also see the time evolution of the molecular hydrogen fraction, starting from neutral, atomic gas, in figure 5. In the low pressure run at a metallicity $0.1Z_{\odot}$ *(top left panel)* the H_2 abundance in the fully shielded region takes ~ 1 Gyr to reach equilibrium. This time-scale is shorter in the high pressure runs and at higher metallicity. At the high pressure and solar metallicity *(bottom right panel)*, the H_2 abundance already reaches equilibrium after ~ 1 Myr.

5 COMPARISON WITH PUBLISHED APPROXIMATIONS FOR H_2 FORMATION

The connection between gas surface density and star formation rate density is well established observationally, both averaged over galactic scales (e.g. Kennicutt 1989, 1998) and also in observations that are spatially resolved on ∼kpc scales (Wong & Blitz 2002; Heyer et al. 2004; Schuster et al. 2007), although at smaller scales, comparable to giant molecular clouds ($\lesssim 100$ pc), this relation breaks down (e.g. Onodera et al. 2010). It has emerged more recently that star formation correlates more strongly with the molecular than with the atomic or total gas content (e.g. Kennicutt et al. 2007; Leroy et al. 2008; Bigiel et al. 2008, 2010), although the more fundamental correlation may in fact be with the cold gas content (Schaye 2004; Krumholz et al. 2011; Glover & Clark 2012).

This important observational link between molecular gas and star formation has motivated several new models and prescriptions for following the H_2 fraction of gas in hydrodynamic simulations. These studies aim to use a more physical prescription for star formation and to investigate its consequence for galactic environments that are not covered by current observations, such as very low metallicity environments at high redshifts. Some of these prescriptions utilise very simple chemical models that include the formation of molecular hydrogen on dust grains and its photodissociation by Lyman Werner radiation to follow the non-equilibrium H_2 fraction (e.g. Gnedin et al. 2009; Christensen et al. 2012). Others use approximate analytic models to predict the H_2 content of a cloud from its physical parameters such as the dust optical depth and incident photodissociating radiation field (e.g. Krumholz et al. 2008, 2009; McKee & Krumholz 2010), which can then be applied to gas particles/cells in hydrodynamic simulations (e.g. Krumholz & Gnedin 2011; Halle & Combes 2013).

In this section we compare the molecular hydrogen fractions predicted by some of these models with our chemical network. We begin by introducing the molecular hydrogen models from the literature that we will compare our chemical network to, and then we present our results.

5.1 Gnedin09 model

Gnedin et al. (2009) present a simple prescription to follow the non-equilibrium evolution of the molecular hydrogen fraction in hydrodynamic simulations, which has been implemented in cosmological Adaptive Mesh Refinement (AMR) simulations (Gnedin & Kravtsov 2010), and was also adapted by Christensen et al. (2012) for cosmological Smoothed Particle Hydrodynamics (SPH) simulations. This model includes the formation of H_2 on dust grains, photodissociation by Lyman Werner radiation, shielding by both dust and H_2, and a small number of gas phase reactions that become important in the dust-free regime (we use the five gas phase reactions suggested by Christensen et al.

2012; see below). The evolution of the neutral and molecular hydrogen fractions, $x_{\rm HI}$ and $x_{\rm H_2}$, can then be described by the following rate equations:

$$\dot{x}_{\rm HI} = R(T) n_e x_{\rm HII} - S_{\rm d} x_{\rm HI} \Gamma_{\rm HI} - C_{\rm HI} x_{\rm HI} n_{\rm e} - 2\dot{x}_{\rm H_2}, \quad (5.1)$$

$$\dot{x}_{\rm H_2} = R_{\rm d} n_{\rm H_{tot}} x_{\rm HI} (x_{\rm HI} + 2x_{\rm H_2}) - S_{\rm d} S_{\rm self}^{\rm H_2} \Gamma_{\rm H_2}^{\rm LW} + \dot{x}_{\rm H_2}^{\rm gp}. \quad (5.2)$$

Following Christensen et al. (2012), we have also included the collisional ionisation of HI, $C_{\rm HI}$, in the above equations, even though it was omitted by Gnedin et al. (2009). $R(T)$ is the recombination rate of HII, $\Gamma_{\rm HI}$ is the photoionisation rate of HI and $\Gamma_{\rm H_2}^{\rm LW}$ is the photodissociation rate of H_2 by Lyman Werner radiation. For the gas phase reactions, $\dot{x}_{\rm H_2}^{\rm gp}$, we include the five reactions suggested by Christensen et al. (2012): the formation of H_2 via H^- and its collisional dissociation via H_2, HI, HII and e^-, with the abundance of H^- assumed to be in chemical equilibrium, as given by equation (27) of Abel et al. (1997).

Gnedin et al. (2009) use the H_2 self-shielding factor $S_{\rm self}^{\rm H_2}$ from Draine & Bertoldi (1996), albeit with different parameters. They find that using $\omega_{\rm H_2} = 0.2$ and a constant Doppler broadening parameter of $b = 1\,{\rm km\,s^{-1}}$ in equation 3.11, along with the original value of $\alpha = 2$, produces better agreement between their model and observations. This choice of parameters results in weaker H_2 self-shielding compared to our temperature-dependent self-shielding function (equations 3.12 to 3.15) for the same value of b. However, in our fiducial model we include a turbulent Doppler broadening parameter of $b_{\rm turb} = 7.1\,{\rm km\,s^{-1}}$, which makes the self-shielding weaker in our model than in the Gnedin09 model at intermediate H_2 column densities ($10^{14}\,{\rm cm^{-2}} \lesssim {\rm N_{H_2}} \lesssim 10^{16}\,{\rm cm^{-2}}$).

The dust shielding factor $S_{\rm d}$ is given in equation 3.4, except that Gnedin et al. (2009) use an effective dust area per hydrogen atom of $\sigma_{\rm d,eff} = \gamma_{\rm d}^{\rm H_2} A_v / N_{\rm H_{tot}} = 4 \times 10^{-21}\,{\rm cm^2}$. This is a factor of 2.7 larger than the value that we use. Also, unlike us, they use the same dust shielding factor for both H_2 and HI.

For the rate of formation of H_2 on dust grains ($R_{\rm d}$), Gnedin et al. (2009) use a rate that was derived from observations by Wolfire et al. (2008), scaled linearly with the metallicity and multiplied by a clumping factor C_ρ that accounts for the fact that there may be structure within the gas below the resolution limit, and that molecular hydrogen will preferentially form in the higher density regions:

$$R_{\rm d} = 3.5 \times 10^{-17} Z/Z_\odot C_\rho\,{\rm cm^3 s^{-1}}. \quad (5.3)$$

Gnedin et al. (2009) use a clumping factor $C_\rho = 30$, but in our comparisons we consider spatially resolved, one-dimensional simulations of an illuminated slab of gas. Therefore, for these comparisons we shall take $C_\rho = 1$. For gas temperatures $10\,{\rm K} < T < 10^3\,{\rm K}$, the rate in equation 5.3 is within a factor ~ 2 of the value used in our model, taken from Cazaux & Tielens (2002) with a dust temperature of 10 K. However, above 10^3 K the H_2 formation rate on dust grains in our model decreases. This temperature dependence is not included in the Gnedin09 model.

Finally, the abundances of electrons and HII can be calculated from constraint equations.

Gnedin & Kravtsov (2011) expand the Gnedin09 model to include the Helium chemistry. There are also other examples in the literature of methods that follow the non-equilibrium evolution of H_2 using simplified chemical models. For example, Bergin et al. (2004) present a model for the evolution of molecular hydrogen that includes the formation of H_2 on dust grains and its dissociation by Lyman Werner radiation and cosmic rays, although they do not include the gas phase reactions (see their equation A1). The model of Bergin et al. (2004) has been used to investigate the formation of molecular clouds in galactic discs (e.g. Dobbs & Bonnell 2008; Khoperskov et al. 2013). We only consider the Gnedin09 chemical model in this section.

5.2 KMT model

Krumholz et al. (2008, 2009) and McKee & Krumholz (2010) develop a simple analytic model that considers a spherical gas cloud that is immersed in an isotropic radiation field. By solving approximately the radiative transfer equation with shielding of the Lyman Werner radiation by dust and H_2 to obtain the radial dependence of the radiation field, and then balancing the photodissociation of molecular hydrogen against its formation on dust grains, they derive simple analytic estimates for the size of the fully molecular region of the cloud, and hence for its molecular fraction in chemical equilibrium.

We use equation (93) of McKee & Krumholz (2010) to calculate the mean equilibrium H_2 fraction, $f_{\rm H_2}$, of a gas cloud:

$$f_{\rm H_2} = 1 - \left(\frac{3}{4}\right) \frac{s}{1 + 0.25s}, \quad (5.4)$$

where s is given by their equation (91):

$$s = \frac{\ln(1 + 0.6\chi + 0.01\chi^2)}{0.6\tau_c}, \quad (5.5)$$

where χ and τ_c are dimensionless parameters of their model, which represent a measure of the incident Lyman Werner radiation field and the dust optical depth to the centre of the cloud respectively. They are given by their equations (9) and (86):

$$\chi = 71 \left(\frac{\sigma_{\rm d,-21}}{R_{\rm d,-16.5}}\right) \frac{G_0^{'}}{(n_{\rm H}/{\rm cm^{-3}})}, \quad (5.6)$$

$$\tau_c = \frac{3}{4} \left(\frac{\Sigma \sigma_{\rm d}}{\mu_{\rm H}}\right) = \sigma_{\rm d} N_{\rm H_{tot}}, \quad (5.7)$$

where $\sigma_{\rm d,-21} = \sigma_{\rm d}/10^{-21}\,{\rm cm^2}$, $\sigma_{\rm d}$ is the cross-sectional area of dust grains available to absorb photons (Krumholz et al. 2009 use $\sigma_{\rm d} = 10^{-21} Z/Z_\odot\,{\rm cm^2}$), and $R_{\rm d,-16.5} = R_{\rm d}/10^{-16.5}{\rm cm^3\,s^{-1}}$, where $R_{\rm d}$ is the rate coefficient for H_2 formation on dust grains. For the latter, McKee & Krumholz (2010) use an observationally determined value from Draine & Bertoldi (1996), multiplied by the metallicity: $R_{\rm d,-16.5} = Z/Z_\odot$. Krumholz & Gnedin (2011) also boost $R_{\rm d,-16.5}$ by the clumping factor C_ρ, whereas Krumholz (2013) multiply τ_c by the clumping factor, but we take $C_\rho = 1$. $G_0^{'}$ is the number density of dissociating photons in the Lyman Werner

band, normalised to the value from Draine (1978) for the Milky Way. For the Black (1987) interstellar radiation field that we consider here, $G_0^{'} = 0.803$. $n_{\rm H}$ is the total hydrogen number density, $\mu_{\rm H}$ is the mean mass per hydrogen nucleus, Σ is the average surface density of the spherical cloud and $N_{\rm H_{tot}}$ is the total hydrogen column density from the edge of the cloud to its centre.

Krumholz et al. (2009) and Krumholz (2013) demonstrate that the molecular gas content predicted by this model is in agreement with various extragalactic observations and with observations of molecular clouds within the Milky Way, for particular values of the clumping factor C_ρ and assumptions about the radiation field and/or density. For example, Krumholz et al. (2009) assume that the ratio of the radiation field to the density, $G_0^{'}/n_{\rm H}$, is set by the minimum density of the cold neutral medium required for the ISM to be in two-phase equilibrium. As shown in their equation 7, the ratio $G_0^{'}/n_{\rm H}$ then depends only on metallicity under this assumption. Krumholz (2013) extends the approach of Krumholz et al. (2009) by assuming that, as $G_0^{'} \rightarrow 0$, the density $n_{\rm H}$ reaches a minimum floor, which is required to ensure that the thermal pressure of the ISM is able to maintain hydrostatic equilibrium in the disc. This becomes important in the molecule-poor regime. In contrast, the runs that we present below use a constant incident radiation field (the Black 1987 interstellar radiation field) and assume a density profile such that the gas pressure is constant throughout the cloud.

Krumholz & Gnedin (2011) implement this model in cosmological AMR simulations to estimate the equilibrium H_2 fraction of each gas cell. Halle & Combes (2013) also implement the KMT model in SPH simulations of isolated disc galaxies to investigate the role that the cold molecular phase of the ISM plays in star formation and as a gas reservoir in the outer disc.

5.3 Results

In Figure 5 we compare the molecular abundances from our model *(coloured solid curves)* with the simpler Gnedin09 *(coloured dashed curves)* and KMT *(black solid curves)* models described above. These were calculated using temperature and density profiles that are in thermal and pressure equilibrium. We use two different pressures, $P/k_{\rm B} = 10^3\,{\rm cm^{-3}\,K}$ *(top row)* and $P/k_{\rm B} = 10^5\,{\rm cm^{-3}\,K}$ *(bottom row)*, and two metallicities, $Z = 0.1 Z_\odot$ *(left column)* and $Z_\odot$ *(right column)*. The colour encodes the time evolution in our model and the Gnedin09 model, starting from fully neutral, atomic gas (KMT is an equilibrium model). In figures 2-4 we showed the abundances in each gas cell, but figure 5 shows the cumulative molecular fraction, i.e. the fraction of all hydrogen atoms that is in H_2 up to a given column density. This allows us to compare our results to the KMT model, in which the specified column density is measured to the centre of a spherical cloud, and then the H_2 fraction, $f_{\rm H_2}$, is the fraction of gas in the entire cloud that is molecular, rather than the fraction of molecular gas at that column density. However, this is still not entirely equivalent to our model as we assume a plane-parallel geometry, whereas the KMT model assumes a spherical geometry.

In the low pressure runs, the final molecular fractions predicted by our model generally agree well with both the Gnedin09 and the KMT models. The time evolution of the H_2 fraction in our model and the Gnedin09 model are also in good agreement. The largest discrepancy in the equilibrium abundance is in the fully shielded region at low metallicity (top left panel of figure 5), where the equilibrium H_2 fraction in our model is a factor of two lower than that predicted by the Gnedin09 and KMT models. This is due to cosmic ray dissociation of H_2, which lowers the H_2 abundance but is not included in the Gnedin09 or KMT models.

In the high pressure runs the HI-H_2 transition occurs at a slightly lower column density than in the KMT model. For example, at solar metallicity (bottom right panel of figure 5), we predict that $f_{\rm H_2} = 0.5$ at $N_{\rm H_{tot}} = 2.2 \times 10^{19}\,{\rm cm^{-2}}$, compared to $N_{\rm H_{tot}} = 3.0 \times 10^{19}\,{\rm cm^{-2}}$ for KMT. In the Gnedin09 model, the HI-H_2 transition is noticeably flatter at high pressure than in our model or in the KMT model. The H_2 fraction starts to increase at a lower column density in the Gnedin09 model than in the other two models, but the column density at which $f_{\rm H_2} = 0.5$ is higher, e.g. $N_{\rm H_{tot}} = 5.6 \times 10^{19}\,{\rm cm^{-2}}$ at solar metallicity. This difference is due to the different H_2 self-shielding function that is used in the Gnedin09 model.

Krumholz & Gnedin (2011) compare the KMT and Gnedin09 models in a hydrodynamic simulation of a Milky Way progenitor galaxy. For the Gnedin09 model, they include the changes described in Gnedin & Kravtsov (2011), which adds Helium chemistry to the chemical network, and uses the simpler power-law H_2 self-shielding function given in equation 36 of Draine & Bertoldi (1996). They find that the molecular fractions predicted by the two models are in excellent agreement for metallicities $Z > 10^{-2}\,Z_\odot$, with discrepancies at lower metallicities likely due to time-dependent effects. This is consistent with what we find in the top row of figure 5 for the low pressure runs. In contrast, the high pressure runs in the bottom row of figure 5 show poor agreement between the KMT and Gnedin09 models. However, this high pressure was chosen to reproduce densities typical of molecular clouds ($n_{\rm H_{tot}} \sim 10^3\,{\rm cm^{-2}}$) in the fully shielded region, and it produces unusually high densities in the low column density region ($n_{\rm H_{tot}} \sim 10\,{\rm cm^{-2}}$). Such regions of high density and low column density were not probed by the simulation of Krumholz & Gnedin (2011), and are likely to be rare in realistic galactic environments. Therefore, the discrepancies that we see in figure 5 do not contradict the results of Krumholz & Gnedin (2011).

In all three models the HI-H_2 transition occurs at a lower column density at higher metallicity and at higher pressure. As described in section 4.3, these trends are driven by H_2 self-shielding, because the H_2 fraction in the photodissociated region is higher at high metallicity and at high pressure. From the colour bars in each panel of figure 5, we also see that the molecular fractions reach chemical equilibrium faster at higher metallicity and higher pressure.

To highlight the impact that H_2 self-shielding has on the HI-H_2 transition, we repeated the above calculations with H_2 self-shielding switched off in our model and in the Gnedin09 model. These results are shown in figure 6. Note that the KMT prediction in this figure still includes self-shielding and thus is identical to figure 5. We include the KMT prediction as a point of reference to allow for easier comparison between the two figures.

In the runs with a low pressure the total hydrogen col-

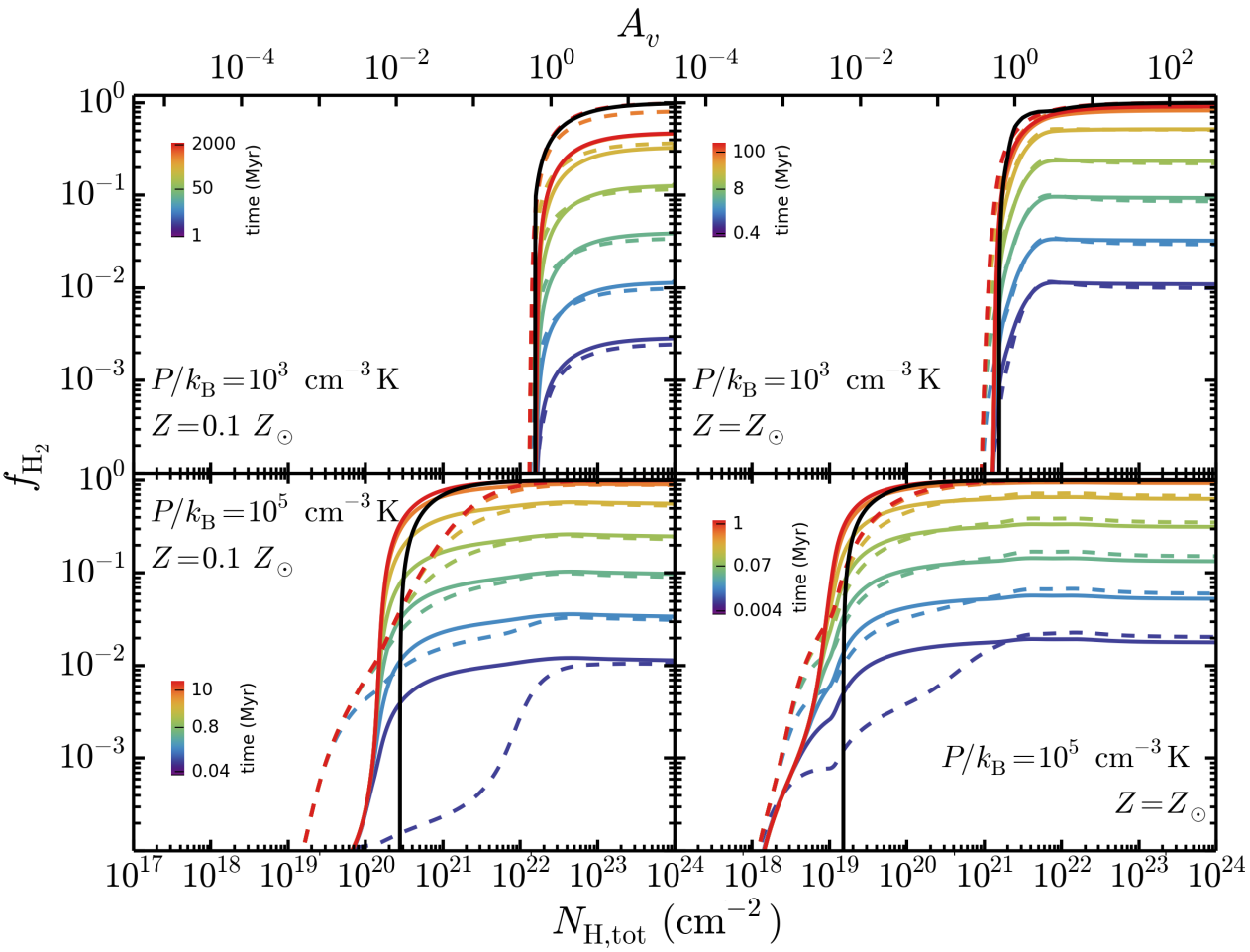

Figure 5. Comparison of the cumulative molecular hydrogen fraction, plotted as a function of total hydrogen column density, as predicted by our chemical model *(solid coloured curves)*, the Gnedin09 model *(dashed coloured curves)* and the equilibrium KMT model *(solid black curve)*. The coloured lines show the non-equilibrium evolution measured at logarithmic time intervals, as indicated by the colour bars, until the simulation reaches chemical equilibrium (red curves). Each run was calculated with a density and temperature profile in pressure and thermal equilibrium, with a pressure $P/k_{\rm B} = 10^3\,{\rm cm^{-3}\,K}$ *(top row)* and $P/k_{\rm B} = 10^5\,{\rm cm^{-3}\,K}$ *(bottom row)*. We used a metallicity $0.1Z_\odot$ *(left column)* and $Z_\odot$ *(right column)*. At low pressure the agreement between the different models is good, except that in the low metallicity run (top left panel), cosmic ray dissociation of H_2, which was not included in the KMT and Gnedin09 models, reduces the equilibrium H_2 fraction by a factor of two in the fully shielded region. At high pressure the differences between the models are substantial.

umn density at the HI-H_2 transition, at which $f_{\rm H_2} = 0.5$, increases by a factor of a few in our model when H_2 self-shielding is omitted (e.g. from $N_{\rm H_{tot}} \approx 3.4 \times 10^{21}\,{\rm cm^{-2}}$ to $N_{\rm H_{tot}} \approx 1.6 \times 10^{22}\,{\rm cm^{-2}}$ at solar metallicity). In the high pressure runs it increases by more than two orders of magnitude (e.g. from $N_{\rm H_{tot}} \approx 2.2 \times 10^{19}\,{\rm cm^{-2}}$ to $N_{\rm H_{tot}} \approx 7.9 \times 10^{21}\,{\rm cm^{-2}}$ at solar metallicity). Furthermore, the dependence of the transition column density on pressure in our model is weaker once we switch off H_2 self-shielding, and it scales approximately linearly with metallicity Z because we assume that $A_v/N_{\rm H_{tot}} \propto Z$.

The total hydrogen column density of the HI-H_2 transition predicted by the Gnedin09 model also increases when we switch off H_2 self-shielding, although there is an offset towards lower column densities by a factor of ~ 3 compared to our model in all panels of figure 6. This offset occurs because the Gnedin09 model uses an effective dust cross section per hydrogen atom of $\sigma_{\rm d,eff} = 4 \times 10^{21}\,{\rm cm^{-2}}$, which is larger than the value that we use ($\sigma_{\rm d,eff} = 1.5 \times 10^{-21}\,{\rm cm^{-2}}$). However, the Gnedin & Kravtsov (2011) implementation of the Gnedin09 model uses a value of $\sigma_{\rm d,eff} = 2 \times 10^{-21}\,{\rm cm^{-2}}$, which is closer to the value that we use.

6 CONCLUSIONS

We have extended the thermo-chemical model from paper I to account for gas that becomes shielded from the incident UV radiation field. We attenuate the photoionisation, photodissociation and photoheating rates by dust and by the gas itself, including absorption by HI, H_2, HeI, HeII and CO where appropriate. For the self-shielding of H_2, we use a new temperature-dependent analytic approximation that we fit to the suppression of the H_2 photodissociation rate predicted by CLOUDY as a function of H_2 column density (see appendix B). Using this model, we investigated the impact

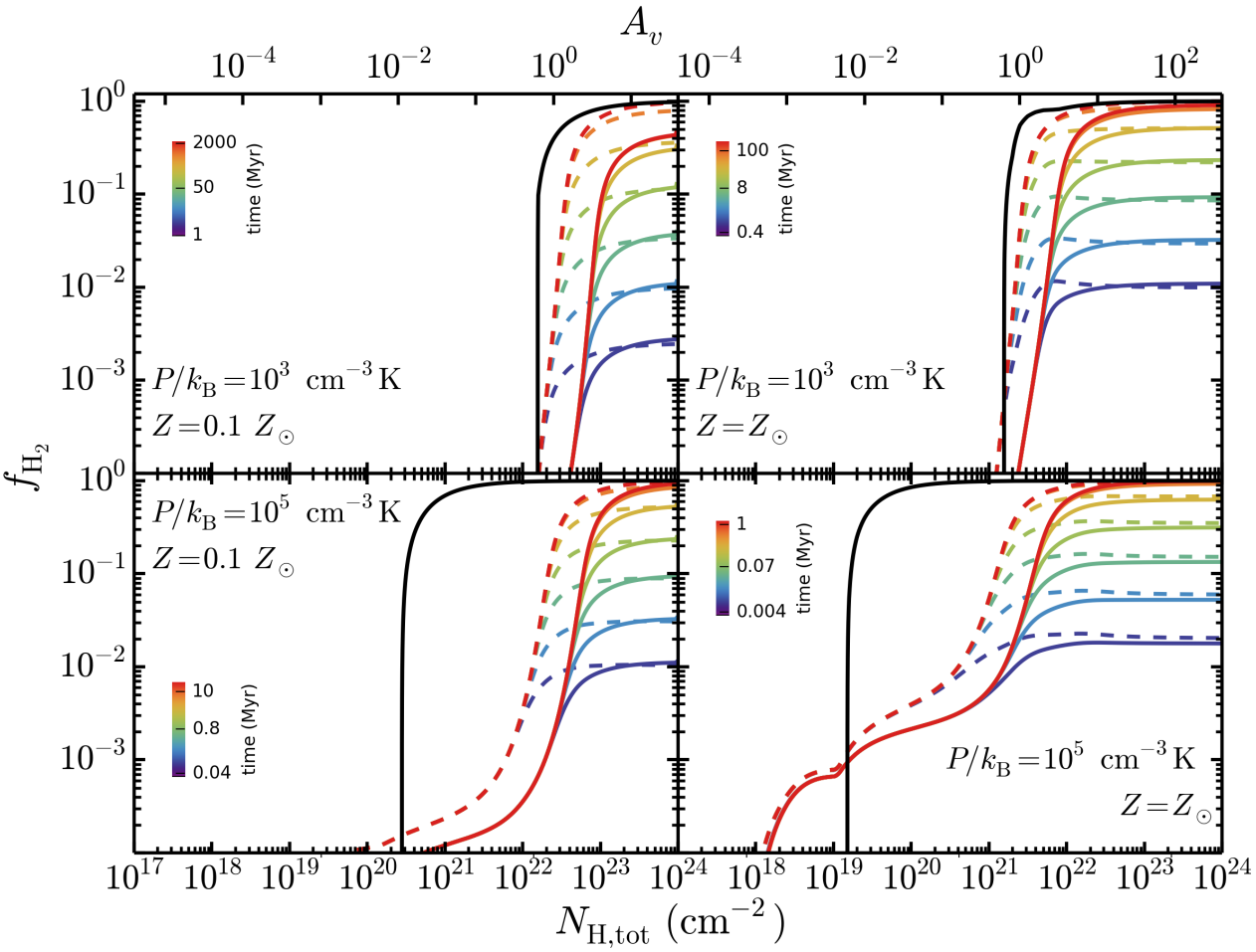

Figure 6. As figure 5, but with H_2 self-shielding switched off for both our model and the Gnedin09 model. The KMT model still includes H_2 self-shielding in this figure and is therefore identical in figure 5. We include the KMT prediction here as a reference point for easier comparison between the two figures. The transition column density is substantially higher in Gnedin09 and our model when we switch off H_2 self-shielding, which confirms that the self-shielding of molecular hydrogen determines the HI-H_2 transition in these models in figure 5. The offset between our model and the Gnedin09 model arises because we use different values for the effective dust cross section per hydrogen atom, $\sigma_{\rm d,eff}$.

that shielding of both the photoionising and the photodissociating radiation has on the chemistry and the cooling properties of the gas.

We have performed a series of one-dimensional calculations of a plane-parallel slab of gas illuminated by the Black (1987) interstellar radiation field at constant density. Comparing equilibrium abundances and cooling and heating rates as a function of column density with CLOUDY, we generally find good agreement. At $n_{\rm H_{tot}} = 100\,{\rm cm^{-3}}$, solar metallicity and a constant temperature $T = 300$ K, we find that the HI-H_2 transition occurs at a somewhat lower column density in our model than in CLOUDY's big H2 model, with a molecular hydrogen fraction $x_{\rm H_2} = 0.5$ at $N_{\rm H_{tot}} \approx 8.1 \times 10^{19}\,{\rm cm^{-2}}$ in our model, compared to $N_{\rm H_{tot}} \approx 2.8 \times 10^{20}\,{\rm cm^{-2}}$ in CLOUDY (see figure 2). However, CLOUDY's small H2 model predicts an HI-H_2 transition column density that is closer to our value, with $x_{\rm H_2} = 0.5$ at $N_{\rm H_{tot}} \approx 1.1 \times 10^{20}\,{\rm cm^{-2}}$.

Our model predicts that the HI-H_2 transition is determined by H_2 self-shielding, as the residual molecular hydrogen fraction in the photodissociated region at low column densities is sufficient for self-shielding to become important before dust shielding. As the photodissociation rate is slightly lower in our model than in the big H2 model of CLOUDY, the H_2 fraction at low column densities is slightly higher in our model. This explains why the transition column density is somewhat lower in our model compared to the CLOUDY big H2 model. The importance of H_2 self-shielding also means that the molecular hydrogen transition is sensitive to turbulence, which can suppress self-shielding. The transition for carbon to form CO is primarily triggered by dust shielding and thus occurs at a higher column density, $N_{\rm H_{tot}} \sim 10^{22}\,{\rm cm^{-2}}$.

We also consider gas clouds with temperature and density profiles that are in thermal and pressure equilibrium, which is more realistic for a two-phase ISM than a gas cloud with constant temperature and density throughout. The effect of H_2 self-shielding is weaker in these examples due to the lower densities in the photodissociated region (see figure 4). However, the HI-H_2 transition is still determined by self-shielding, which becomes more important in runs with higher pressure (and hence higher densities).

The HI-H_2 transition occurs at a lower total column density for higher density (or equivalently, for higher pressure if the cloud is in pressure equilibrium) and for higher metallicity (see figure 5). These trends are due to the H_2 self-shielding, because an increase in the density and/or metallicity will increase the H_2 fraction in the photodissociated region, and hence decrease the total column density at which the H_2 becomes self-shielded. The time evolution of the H_2 fraction is also dependent on the density (or pressure) and the metallicity. For a gas cloud with pressure $P/k_B = 10^3\,\mathrm{cm^{-3}\,K}$ and metallicity $0.1Z_\odot$, the molecular hydrogen abundance in the fully shielded region only reaches equilibrium (starting from neutral, atomic initial conditions) after $\sim$ 1 Gyr. This time-scale decreases as the pressure and/or the metallicity increase.

We compare the dominant cooling and heating processes in our low pressure example ($P/k_B = 10^3\,\mathrm{cm^{-3}\,K}$) at solar metallicity, and we find that they form three distinct regions (see figure 4). At low column densities, where the dissociating and ionising radiation flux is still high, cooling is primarily from ionised metals such as SiII, FeII, FeIII and CII, which are balanced by photoheating, primarily from HI. At column densities above $N_{\mathrm{H_{tot}}} \sim 2\times10^{20}\,\mathrm{cm^{-2}}$ the hydrogen-ionising radiation above 1 Ryd becomes significantly attenuated by neutral hydrogen. This reduces the photoheating rates, making photoelectric dust heating the dominant heating mechanism, while CII starts to dominate the cooling rate above $N_{\mathrm{H_{tot}}} \sim 10^{21}\,\mathrm{cm^{-2}}$. It is also in this region that hydrogen becomes fully molecular, driven initially by an increase in the HI abundance and the rising density, and ultimately by self-shielding. Finally, dust shielding attenuates the radiation flux below 1 Ryd at column densities above $N_{\mathrm{H_{tot}}} \sim 10^{21}\,\mathrm{cm^{-2}}$, which strongly cuts off the dust heating rate and also allows CO to form. In this fully shielded region heating is primarily from cosmic rays, while cooling is mostly from CO and H_2.

Finally, we compare the HI-H_2 transition predicted by our one-dimensional plane-parallel slab simulations in thermal and pressure equilibrium with two other prescriptions for molecular hydrogen formation that are already employed in hydrodynamic simulations: the simpler non-equilibrium model of Gnedin et al. (2009) *(Gnedin09)*, and the analytic equilibrium model developed in Krumholz et al. (2008, 2009) and McKee & Krumholz (2010) *(KMT)* (see figure 5).

At low pressure ($P/k_\mathrm{B} = 10^3\,\mathrm{cm^{-3}\,K}$) the equilibrium H_2 fractions predicted by all three models generally agree well, as does the time evolution of the H_2 fraction predicted by our model and the Gnedin09 model. However, at low metallicity ($0.1\ Z_\odot$) cosmic ray dissociation of H_2 reduces the H_2 fraction in the fully shielded region by a factor of two in our model, but cosmic ray dissociation is not included in the KMT or the Gnedin09 models. At high pressure ($P/k_\mathrm{B} = 10^5\,\mathrm{cm^{-3}\,K}$) the HI-$H_2$ transition predicted by our model in chemical equilibrium occurs at a slightly lower column density than in the KMT model (e.g. $f_{\mathrm{H_2}} = 0.5$ at $N_{\mathrm{H_{tot}}} = 2.2\times10^{19}\,\mathrm{cm^{-2}}$ at solar metallicity, compared to $N_{\mathrm{H_{tot}}} = 3.0\times10^{19}\,\mathrm{cm^{-2}}$ in the KMT model). Furthermore, the HI-H_2 transition at this high pressure is flatter in the Gnedin09 model than in our model or the KMT model, due to the different H_2 self-shielding function that they use.

ACKNOWLEDGMENTS

We thank Ewine van Dishoeck for useful discussions. We gratefully acknowledge support from Marie Curie Training Network CosmoComp (PITN-GA-2009- 238356) and from the European Research Council under the European Union's Seventh Framework Programme (FP7/2007-2013) / ERC Grant agreement 278594-GasAroundGalaxies.

REFERENCES

Abel T., Anninos P., Zhang Y., Norman M. L., 1997, NewA, 2, 181
Bergin E. A., Hartmann L. W., Raymond J. C., Ballesteros-Paredes J., 2004, ApJ, 612, 921
Bigiel F., Leroy A., Walter F., Brinks E., de Blok W. J. G., Madore B., Thornley M. D., 2008, AJ, 136, 2846
Bigiel F., Walter F., Blitz L., Brinks E., de Blok W. J. G., Madore B. F., 2010, AJ, 140, 1194
Black J. H., 1987, ASSL, 134, 731
Cazaux S., Tielens A. G. G. M., 2002, ApJ, 575, L29
Ceverino D., Klypin A., 2009, ApJ, 695, 292
Christensen C., Quinn T., Governato F., Stilp A., Shen S., Wadsley J., 2012, MNRAS, 425, 3058
Dere K. P., Landi E., Mason H. E., Monsignori Fossi B. C., Young P. R., 1997, A&AS, 125, 149
Dobbs C. L., Bonnell I. A., 2008, MNRAS, 385, 1893
Draine B. T., 1978, ApJS, 36, 595
Draine B. T., Bertoldi F., 1996, ApJ, 468, 269
Elwert T., Ferland G. J., Henney W. J., Williams R. J. R., 2005, IAU Symposium, 235, 132
Federman S. R., Rawlings J. M. C., Taylor S. D., Williams D. A., 1996, MNRAS, 279, L41
Ferland G. J., Korista K.T., Verner D.A., Ferguson J.W., Kingdon J.B., Verner E.M., 1998, PASP, 110, 761
Ferland G. J., Porter R. L., van Hoof P. A. M., Williams R. J. R., Abel N. P., Lykins M. L., Shaw G., Henney W. J., Stancil P. C., 2013, RMxAA, 49, 137
Glover S. C. O., Jappsen A.-K., 2007, ApJ, 666, 1
Glover S. C. O., Abel T., 2008, MNRAS, 388, 1627
Glover S. C. O., Federrath C., Mac Low M.-M., Klessen R. S., 2010, MNRAS, 404, 2
Glover S. C. O., Clark P. C., 2012, MNRAS, 421, 9
Gnat O., Sternberg A., 2007, ApJS, 168, 213
Gnedin N. Y., Tassis K., Kravtsov A. V., 2009, ApJ, 697, 55 (Gnedin09)
Gnedin N. Y., Kravtsov A. V., 2010, ApJ, 714, 287
Gnedin N. Y., Kravtsov A. V., 2011, ApJ, 728, 88
Governato F., Brook C., Mayer L., Brooks A., Rhee G., Wadsley J., Jonsson P., Willman B., Stinson G., Quinn T., Madau P., 2010, Nature, 463, 203
Haardt F., Madau P., 2001, in Neumann D. M., Tran J. T. V., eds, XXIst Moriond Astrophys. Meeting, Clusters of Galaxies and the High Redshift Universe Observed in X-rays Editions Frontieres, Paris, p. 6
Halle A., Combes F., 2013, A&A, 559, 55
Heyer M. H., Corbelli E., Schneider S. E., Young J. S., 2004, ApJ, 602, 723
Hopkins P. F., Kereš D., Onorbe J., Faucher-Giguere C.-A., Quataert E., Murray N., Bullock J. S., 2013, 2013arXiv1311.2073

Kaastra J. S., Mewe R., 1993, A&AS, 97, 443
Kafatos M., 1973, ApJ, 182, 433
Kennicutt R. C. Jr., 1989, ApJ, 344, 685
Kennicutt R. C. Jr., 1998, ApJ, 498, 541
Kennicutt R. C. Jr. et al., 2007, ApJ, 671, 333
Khoperskov S. A., Vasiliev E. O., Sobolev A. M., Khoperskov A. V., 2013, MNRAS, 428, 2311
Krumholz M. R., McKee C. F., Tumlinson J., 2008, ApJ, 689, 865 (KMT)
Krumholz M. R., McKee C. F., Tumlinson J., 2009, ApJ, 693, 216
Krumholz M. R., Leroy A. K., McKee C. F., 2011, ApJ, 731, 25
Krumholz M. R., Gnedin N. Y., 2011, ApJ, 729, 36
Krumholz M. R., 2012, ApJ, 759, 9
Krumholz M. R., 2013, MNRAS, 436, 2747
Landi E., Young P. R., Dere K. P., Del Zanna G., Mason H. E., 2013, ApJS, 763, 86
Langer W. D., 1978, ApJ, 225, 860
Lee H.-H., Herbst E., Pineau des Forêts G., Roueff E., Le Bourlot J., 1996, A&A, 311, 690
Leroy A., Walter F., Bigiel F., Brinks E., de Blok W. J. G., Madore B., 2008, AJ, 136, 2782
Le Teuff Y. H., Millar T. J., Marwick A. J., 2000, A&AS, 146, 157
Lotz W., 1967, ApJS, 14, 207
Martin P. G., Whittet D. C. B., 1990, ApJ, 357, 113
McKee C. F., Krumholz M. R., 2010, ApJ, 709, 308
Onodera S., Kuno N., Tosaki T., Kohno K., Nakanishi K., Sawada T., Muraoka K., Komugi S., Miura R., Kaneko H., Hirota A., Kawabe R., 2010, ApJ, 722, 127
Oppenheimer B. D., Schaye J., 2013a, MNRAS, 434, 1043
Oppenheimer B. D., Schaye J., 2013b, MNRAS, 434, 1063
Pelupessy F. I., Papadopoulos P. P., van der Werf P., 2006, ApJ, 645, 1024
Rahmati A., Pawlik A. H., Raičevič M., Schaye J., 2013, MNRAS, 430, 2427
Richings A. J., Schaye J., & Oppenheimer B. D., 2014, arXiv:1401.4719 (Paper I)
Schaye J., 2001a, ApJ, 559, 507
Schaye J., 2001b, ApJ, 562, L95
Schaye J., 2004, ApJ, 609, 667
Schaye J., Dalla Vecchia C., Booth C. M., Wiersma R. P. C., Theuns T., Haas M. R., Bertone S., Duffy A. R., McCarthy I. G., van de Voort F., 2010, MNRAS, 402, 1536
Schuster K. F., Kramer C., Hitschfeld M., Garcia-Burillo S., Mookerjea B., 2007, A&A, 461, 143
Sheffer Y., Rogers M., Federman S. R., Abel N. P., Gredel R., Lambert D. L., Shaw G., 2008, ApJ, 687, 1075
Silk J., 1970, ApL, 5, 283
Sobolev V. V., 1957, SvA, 1, 678
Tielens A. G. G. M., Hollenbach D., 1985, ApJ, 291, 722
van Dishoeck E. F., Black J. H., 1986, ApJS, 62, 109
van Dishoeck E. F., Black J. H., 1988, ApJ, 334, 771
van Dishoeck E. F., Jonkheid B., van Hemert M. C., 2006, Faraday Discuss., 133, 231
Vasiliev E. O., 2013, MNRAS, 431, 638
Verner D. A., Yakovlev D. G., 1995, A&AS, 109, 125
Verner D. A., Ferland G. J., Korista K. T., Yakovlev D. G., 1996, ApJ, 465, 487
Visser R., van Dishoeck E. F., Black J. H., 2009, A&A, 503, 323
Weingartner J. C., Draine B. T., 2001a, ApJ, 563, 842
Weingartner J. C., Draine B. T., 2001b, ApJ, 548, 296
Wiersma R. P. C., Schaye J., Smith B. D., 2009, MNRAS, 393, 99
Williams J. P., Bergin E. A., Caselli P., Myers P. C., Plume R., 1998, ApJ, 503, 689
Wilson T. L., 1999, Rep. Prog. Phys., 62, 143
Wolcott-Green J., Haiman Z., Bryan G. L., 2011, MNRAS, 418, 838
Wolfire M. G., Hollenbach D., McKee C. F., Tielens A. G. G. M., Bakes E. L. O., 1995, ApJ, 443, 152
Wolfire M. G., Tielens A. G. G. M., Hollenbach D. J., Kaufman M. J., 2008, ApJ, 680, 384
Wolfire M. G., Hollenbach D., McKee C. F., ApJ, 716, 1191
Wong T., Blitz L., 2002, ApJ, 569, 157

APPENDIX A: SHIELDING APPROXIMATIONS

In section 3 we described how we calculate the photoionisation and photoheating rates after the radiation field has been attenuated by a total column density $N_{\mathrm{H_{tot}}}$. To compute the attenuation of the radiation by gas, we include absorption by HI, H_2, HeI and HeII. However, to reduce the number of dimensions in which we tabulate the attenuated rates, H_2 and HeII absorption are included as follows. We assume that the H_2 cross section is three times the HI cross section above the H_2 ionisation energy (15.4 eV), and similarly that the HeII cross section is 0.75 times the HeI cross section above the HeII ionisation energy (54.4 eV). In this section we show the errors that these approximations introduce to the photoionisation rates.

For every species included in our chemical network, we calculate the ratio of the optically thick to optically thin photoionisation rates, S_{gas}, from the Black (1987) radiation field after it has been attenuated purely by H_2. We calculate this exactly using equation 3.5, then we calculate it with our approximation using equation 3.8. In the top panel of figure A1 we show contours of the relative error in S_{gas} that is introduced by our approximation for H_2 absorption, plotted against the threshold energy of each species, E_{thresh}, on the x-axis, and the exact ratio of the optically thick to optically thin rates, S_{exact}, on the y-axis. Blue contours indicate where our approximation underestimates the photoionisation rates and red contours indicate where we overestimate them.

The largest errors seen in the top panel of figure A1 are seen in the blue contours, which show that we underestimate the photoionisation rates of some species by up to 60% at $S_{\mathrm{exact}} \lesssim 10^{-3}$. However, since these errors are found at low values of S_{exact}, the photoionisation rates have already been suppressed and so are unlikely to be important in the chemical network. The more significant errors in this example are shown by the red contours in the top left corner of the top panel of figure A1. These show that we overestimate the photoionisation rates of species with $E_{\mathrm{thresh}} \sim 20$ eV by up to 40% at $S_{\mathrm{exact}} \sim 10^{-1}$.

We also calculated the relative errors in the photoionisation rates when the radiation field is attenuated purely

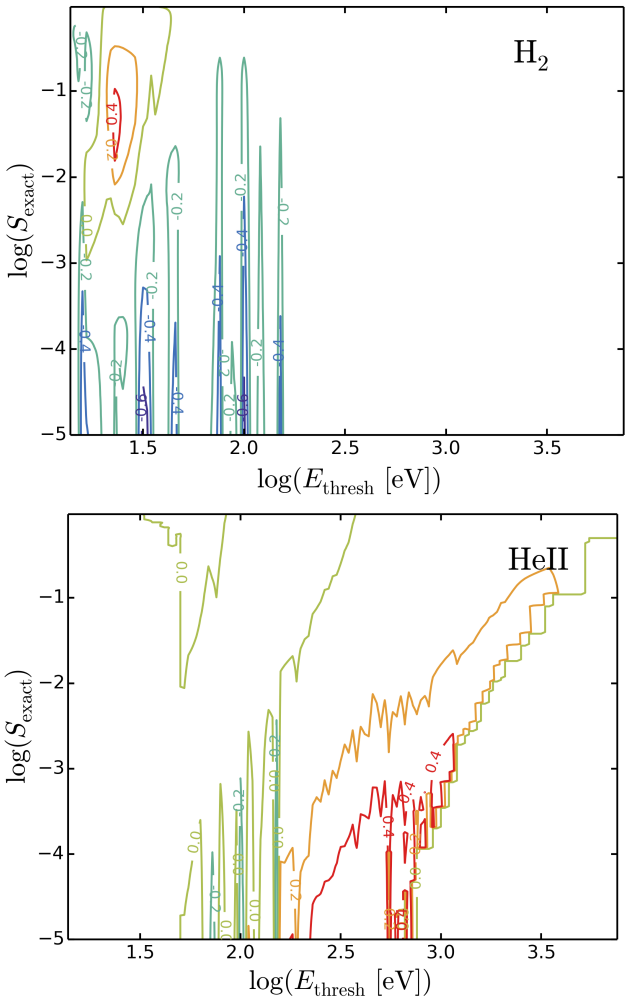

Figure A1. Contours of the relative errors in the ratio of optically thick to optically thin photoionisation rates of all species in our chemical network introduced by our approximations for absorption by H_2 and HeII, as given by equations 3.6, 3.7 and 3.8, in the presence of the Black (1987) interstellar radiation field. These contours are plotted against the threshold energy of each species, $E_{\rm thresh}$, on the x-axis, and the exact ratio of the optically thick to optically thin rates, $S_{\rm exact}$, on the y-axis. A value of $\log S_{\rm exact} = 0$ corresponds to the optically thin limit, and a value of $\log S_{\rm exact} = -\infty$ corresponds to the fully shielded limit. The top panel shows the errors if the radiation is absorbed purely by H_2 and the bottom panel shows if the radiation is absorbed purely by HeII. The largest errors that we see are $\sim 60\%$, but these are rare and are typically found at $S_{\rm exact} \lesssim 10^{-3}$, where the photoionisation rate is already strongly suppressed and so the errors are less important.

by HeII. These are shown in the bottom panel of figure A1. For species with $E_{\rm thresh} < 100$ eV, the errors are below 20%. Larger errors are seen for species with higher threshold energies and mostly in the strongly shielded regime ($S_{\rm exact} \lesssim 10^{-3}$). However, species with such high ionisation energies are unlikely to be found in shielded gas.

The errors in the optically thick photoionisation rates shown in figure A1 were calculated for absorption purely by H_2 or HeII. However, in practice the radiation will typically be absorbed by a combination of the four species that we consider in section 3, including HI and HeI, which we treat exactly. Therefore, figure A1 represents upper limits on the actual errors.

APPENDIX B: H_2 SELF-SHIELDING FUNCTION

In this section we look at the accuracy of the H_2 self-shielding function that we use, as described in section 3.2, by comparing it to the ratio of the optically thick to optically thin H_2 photodissociation rates predicted by CLOUDY as a function of H_2 column density. We consider a plane-parallel slab of gas with primordial abundances that is illuminated from one side by the Black (1987) interstellar radiation field.

Figure B1 shows the suppression factor of the H_2 photodissociation rate due to self-shielding, $S_{\rm self}^{\rm H_2}$, plotted against H_2 column density for five different temperatures in the range $100\,{\rm K} \leqslant {\rm T} \leqslant 5000\,{\rm K}$ (shown in the different rows). The left panels were calculated using purely thermal Doppler broadening, while the right panels include turbulence with a Doppler broadening parameter $b_{\rm turb} = 7.1\,{\rm km\,s^{-1}}$. The black circles show the results from CLOUDY, while the coloured curves show different analytic approximations to the H_2 self-shielding function. The yellow dot-dashed curves show the self-shielding function from Draine & Bertoldi (1996) (DB96), as given in equation 3.11 with $\omega_{\rm H_2} = 0.035$ and $\alpha = 2$, and the blue dotted curves show the suggested modification to this function given by Wolcott-Green et al. (2011) (WG11), with $\alpha = 1.1$. We see that, in the absence of turbulence, the WG11 function gives weaker self-shielding than the DB96 function at intermediate column densities ($10^{15}\,{\rm cm^{-2}} \lesssim {\rm N_{H_2}} \lesssim 10^{17}\,{\rm cm^{-2}}$), by up to a factor ~ 6. However, both of these functions underestimate the strength of the self-shielding in cold gas compared to CLOUDY. For example, at 100 K the value of $S_{\rm self}^{\rm H_2}$ predicted by CLOUDY is a factor of ~ 3 lower than the DB96 and WG11 functions at column densities $N_{\rm H_2} \gtrsim 10^{17}\,{\rm cm^{-2}}$.

To improve the agreement with CLOUDY, we modified the self-shielding function of Draine & Bertoldi (1996) as shown in equation 3.12, then we fitted the parameters $\omega_{\rm H_2}(T)$, $\alpha(T)$ and $N_{\rm crit}(T)$ to the suppression factor $S_{\rm self}^{\rm H_2}$ predicted by CLOUDY as a function of H_2 column density for each temperature separately, including only thermal broadening. To reproduce the temperature dependence of $S_{\rm self}^{\rm H_2}$ seen in CLOUDY we then fitted analytic formulae to these three parameters as a function of temperature. These are given in equations 3.13 to 3.15.

Our best-fitting self-shielding function is shown by the red solid curves in figure B1. In the absence of turbulence, this function agrees with CLOUDY to within 30 per cent at $T = 100$ K for column densities $N_{\rm H_2} < 10^{21}\,{\rm cm^{-2}}$, and to within 60 per cent at $T = 5000$ K for $N_{\rm H_2} < 10^{20}\,{\rm cm^{-2}}$.

To highlight the temperature dependence of $S_{\rm self}^{\rm H_2}$, we also show our best-fitting function using the parameters $\omega_{\rm H_2}(T)$, $\alpha(T)$ and $N_{\rm crit}(T)$ fixed at $T = 100$ K. These are indicated by the green dashed curves in figure B1. This represents the self-shielding function that we would get if we only fitted equation 3.12 at 100 K. Note that the green curves in each panel of figure B1 are not identical as they use the thermal Doppler broadening parameter for the given temperature.

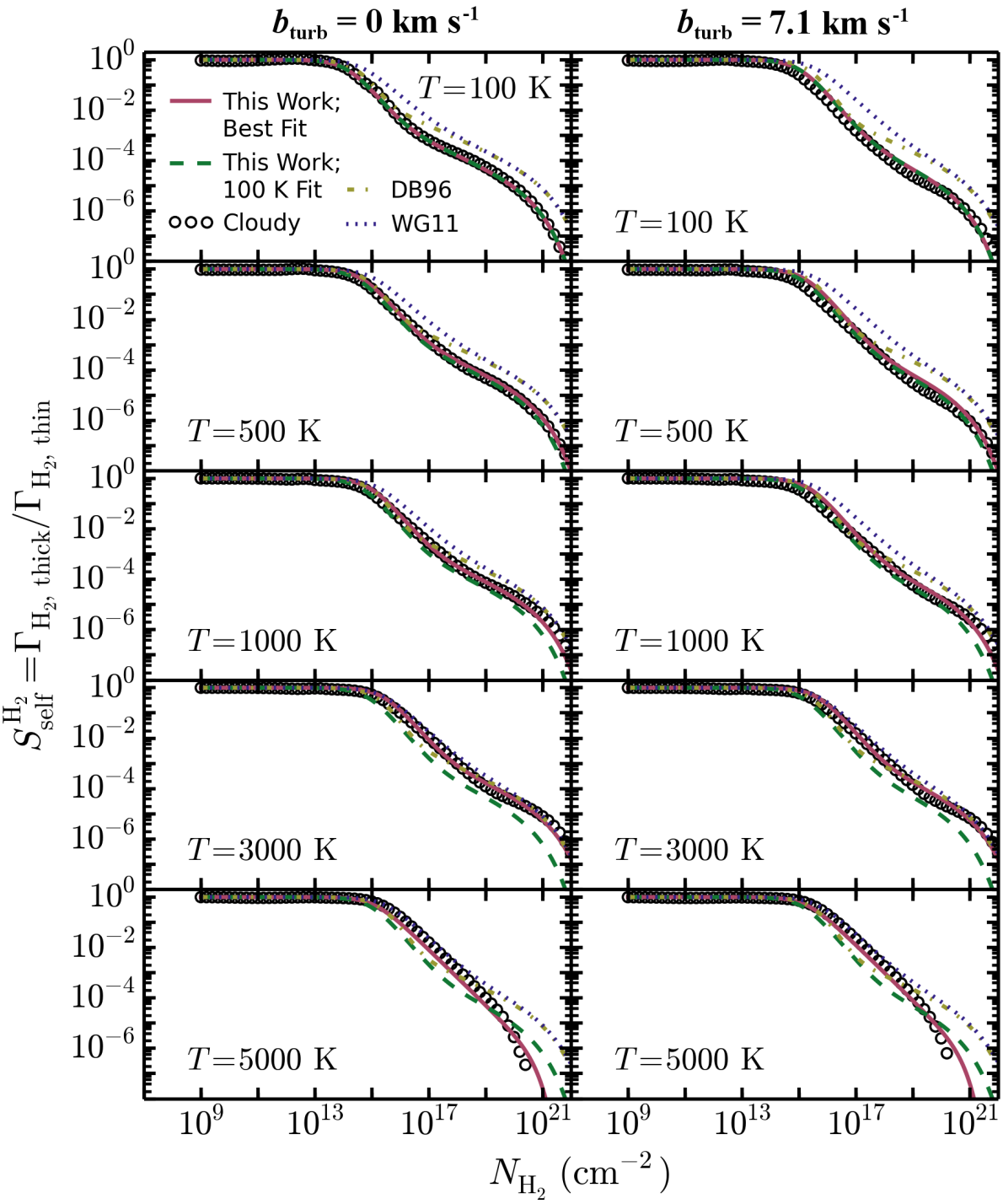

Figure B1. The ratio of the optically thick to optically thin H_2 photodissociation rates, $S^{H_2}_{self}$, plotted against the H_2 column density, N_{H_2}, as predicted by Cloudy *(black circles)*, the self-shielding function of Draine & Bertoldi (1996) *(DB96; yellow dot-dashed curves)*, the self-shielding function of Wolcott-Green et al. (2011) *(WG11; blue dotted curves)*, our self-shielding function fitted to Cloudy at all temperatures *(as given in equations 3.12 to 3.15; red solid curves)*, and our self-shielding function fitted to Cloudy at only 100 K *(green dashed curves)*. Each row shows gas at different temperatures in the range $100\,{\rm K} \leqslant {\rm T} \leqslant 5000\,{\rm K}$. In the left column Doppler broadening is purely thermal, while the right column includes turbulence with a Doppler broadening parameter of $b_{\rm turb} = 7.1\,{\rm km\,s^{-1}}$. In the absence of turbulence, the DB96 and WG11 functions overestimate $S^{H_2}_{self}$ by up to a factor ~ 3 at low temperatures, and they do not reproduce the temperature dependence of $S^{H_2}_{self}$ that is seen in Cloudy. Our best-fitting self-shielding function agrees with Cloudy to within 30 per cent at 100 K for $N_{H_2} < 10^{21}\,{\rm cm^{-2}}$, and at 5000 K it agrees to within 60 per cent for $N_{H_2} < 10^{20}\,{\rm cm^{-2}}$. The agreement between our best-fitting self-shielding function and Cloudy is poorer when turbulence is included, as it was fitted to the purely thermal Doppler broadening case. However, the DB96 and WG11 functions overestimate $S^{H_2}_{self}$ in cold gas by a larger factor when turbulence is included.

Comparing the red and the green curves in figure B1, we see that the self-shielding is weaker at temperatures $500\,\mathrm{K} \lesssim \mathrm{T} \lesssim 3000\,\mathrm{K}$ when we use our full temperature-dependent function (red curves), compared to the function fitted only at 100 K (green curves). This agrees with the trend seen by Wolcott-Green et al. (2011). However, at $T = 5000$ K the shape of the self-shielding function changes, and it becomes steeper than at lower temperatures for high column densities. This results in stronger self-shielding at $N_{\mathrm{H_2}} \gtrsim 10^{19}\,\mathrm{cm}^{-2}$ compared to the fit at 100 K.

Our self-shielding function was fitted to the predictions from Cloudy for gas with purely thermal Doppler broadening. To confirm that our best-fitting self-shielding function is also valid for turbulent gas, we repeated this comparison for gas that includes a turbulent Doppler broadening parameter $b_{\mathrm{turb}} = 7.1\,\mathrm{km\,s}^{-1}$. This comparison is shown in the right panels of figure B1.

When we include turbulence, the agreement between our best-fitting self-shielding function and Cloudy is poorer. For example, at 100 K we overestimate $S_{\mathrm{self}}^{\mathrm{H_2}}$ by up to 90 per cent compared to Cloudy for $10^{15}\,\mathrm{cm}^{-2} < \mathrm{N}_{\mathrm{H_2}} < 10^{20}\,\mathrm{cm}^{-2}$. However, this agreement is still much better than that between Cloudy and the DB96 and WG11 functions. For example, in the same range of column densities the WG11 function overestimates $S_{\mathrm{self}}^{\mathrm{H_2}}$ by up to an order of magnitude at 100 K.